J. Fluid Mech. (2023), *vol*. 968, A28, doi:10.1017/jfm.2023.535

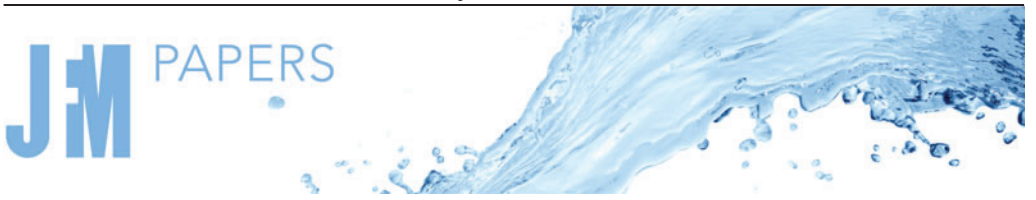

Lagrangian dispersion and averaging behind a two-dimensional gaseous detonation front

Hiroaki Watanabe[1,2,†], Akiko Matsuo[3], Ashwin Chinnayya[2], Noboru Itouyama[1], Akira Kawasaki[1], Ken Matsuoka[1] and Jiro Kasahara[1]

[1]Nagoya University, Furo-cho, Chikusa, Nagoya, Aichi, 464-8603, Japan

[2]Institut Prime UPR 3346 CNRS, ISAE-ENSMA, Université de Poitiers, 1 avenue Clément Ader, BP 40109, 86961 Futuroscope-Chasseneuil CEDEX, France

[3]Keio University, 3-14-1, Hiyoshi, Kohoku-ku, Yokohama, Kanagawa, 223-8522, Japan

(Received 28 November 2022; revised 31 May 2023; accepted 19 June 2023)

Two-dimensional numerical simulations with the particle tracking method were conducted to analyse the dispersion behind the detonation front and its mean structure. The mixtures were $2H_2$–O_2–7Ar and $2H_2$–O_2 of increased irregularity in ambient conditions. The detonation could be described as a two-scale phenomenon, especially for the unstable case. The first scale is related to the main heat release zone, and the second where some classical laws of turbulence remain relevant. The dispersion of the particles was promoted by the fluctuations of the leading shock and its curvature, the presence of the reaction front, and to a lesser extent transverse waves, jets and vortex motion. Indeed, the dispersion and the relative dispersion could be scaled using the reduced activation energy and the χ parameter, respectively, suggesting that the main mechanism driving the dispersion came from the one-dimensional leading shock fluctuations and heat release. The dispersion within the induction time scale was closely related to the cellular structure, particles accumulating along the trajectory of the triple points. Then, after a transient where the fading transverse waves and the vortical motions coming from jets and slip lines were present, the relative dispersion relaxed towards a Richardson–Obukhov regime, especially for the unstable case. Two new Lagrangian Favre average procedures for the gaseous detonation in the instantaneous shock frame were proposed and the mean profiles were compared with those from Eulerian procedure. The characteristic lengths for the detonation were similar, meaning that the Eulerian procedure gave the mean structure with a reasonable accuracy.

Key words: detonations, detonation waves

† Email address for correspondence: watanabe0204@keio.jp

1. Introduction

Detonation is a supersonic premixed combustion wave, which consists of a leading shock wave coupled with a reaction zone (Ficket & Davis 2000; Lee 2008; Zhang 2012), velocity of which is around several millimetres per microsecond. Research on detonation is very active in terms of propulsion applications (Wolanski 2013; Anand & Gutmark 2019) and safety engineering (Oran, Chamberlain & Pekalski 2020). Indeed, pressure increase downstream of the detonation waves is very high. As such, the use of this combustion mode in a chamber may give many advantages over a conventional combustor based on deflagration. The Fickett–Jacob cycle shows that higher thermal efficiency can be theoretically achieved. The compressor and the combustion chamber may thus be more compact. On the other hand, unintentional detonations imply severe damage to humans and goods.

Chapman–Jouguet (CJ) theory can predict the experimental detonation velocity in the ideal case with great accuracy. A control volume embeds the leading shock and the state far from the front where a chemical equilibrium is achieved. The CJ velocity can be determined from the fact that the propagation velocity is minimum. The fact that the CJ velocity can be calculated from the initial conditions and the thermodynamic properties is the so-called Khariton principle, meaning that any material capable of exothermic reaction can detonate without losses from boundaries (Higgins 2012).

Later, Zel'dovich, von Neumann & Döring (ZND) proposed the steady one-dimensional (1-D) model for the detonation structure. The induction reaction is triggered by the adiabatic compression of the leading shock front, after which the exothermic reaction takes place. The reactants are transformed into products, the deflagration zone travelling at the same velocity as that of the shock. Characteristic lengths such as the induction and reaction lengths can thus be estimated by the integration of the ZND model.

In contrast to the ZND model assumptions, detonation has an unsteady, multidimension cellular structure (Gamezo, Desbordes & Oran 1999*a*; Austin 2003; Pintgen *et al.* 2003; Austin, Pintgen & Shepherd 2005; Radulescu *et al.* 2005, 2007; Shepherd 2009; Kiyanda & Higgins 2013). The cornerstone of the latter consists of an incident shock, a Mach stem and a transverse wave, linked by a triple point, the trajectory of which draws a fish-cell-like structure. The stronger Mach stem and the weaker incident shock wave alternate in the propagation direction of the wavefront. The leading shock front velocity fluctuated around 0.9–1.25 and 0.7–1.7 times the CJ velocity in weakly unstable and unstable mixtures, respectively (Gamezo *et al.* 1999*a*). Near the end of the cell, collision of transverse waves, propagating perpendicularly to the leading shocks, may result in very high explosion centres. As a result of all these events, a wide range of distribution of induction, reaction lengths and composition were present, due to the exponential dependence of the chemical reaction rates on temperature (Austin 2003; Pintgen *et al.* 2003; Austin *et al.* 2005).

From unsteady 1-D simulations, Ng *et al.* (2005*a*), Henrick, Aslam & Powers (2006) and Romick, Aslam & Power (2012) showed that the shock pressure followed a period-doubling Feigenbaum scenario, through the increase of the reduced activation, with Abderrahmane, Paquet & Ng (2011) determining that the corresponding chaos was deterministic. Shepherd (2009) argued that the detonation could be statistically tractable. The hydrodynamic thickness x_{HT} is the distance between the leading shock and the mean location of the sonic locus, although the latter oscillated and did not strictly coincide any more with the end of the chemical reaction (Kasimov & Stewart 2004; Stewart & Kasimov 2005). As such, this length can be meant as a measure of the detonation driving zone (Short & Quirk 2018; Chiquete & Short 2019) that embeds in the multidimensional case the leading shock and the sonic surfaces. Moreover, this length could be related to the

dynamic parameters of detonation (Murray & Lee 1983, 1985, 1986; Reynaud, Taileb & Chinnayya 2020).

The hydrodynamic thickness was estimated from both experimental and numerical studies. In experimental studies, the bow shock technique (Vasil'ev *et al.* 1972; Weber & Olivier 2003) or the decay of the pressure signal (Edwards, Jones & Phillips 1976; Jarsalé, Virot & Chinnayya 2016) were used. Its estimation in numerical studies were determined by averaging the flow field (Lee & Radulescu 2005; Radulescu *et al.* 2007) or by shortening the computational domain until the effect of the rarefactions of the Taylor wave were no more effective (Gamezo, Desbordes & Oran 1999*b*; Mi *et al.* 2018). Gamezo *et al.* (1999*a*) investigated the effects of the reduced activation energy on detonation, by comparing the Reynolds averages from simulations with the ZND results. Later, Lee & Radulescu (2005) and Radulescu *et al.* (2007) proposed a Favre averaging procedure in the mean shock frame. They revealed two important characteristic lengths, associated with chemical exothermicity and the slower dissipation of the hydrodynamic fluctuations, which govern the location of the average sonic surface, thus demonstrating the usefulness of the statistical analysis for detonation. Furthermore, Sow, Chinnayya & Hadjadj (2014) proposed the Favre average procedure for the detonation in the non-inertial instantaneous shock frame to take into account the unsteadiness of the shock front. So far, the Favre average procedure to obtain 1-D profiles was applied to planar detonations (Lee & Radulescu 2005; Radulescu *et al.* 2007; Maxwell *et al.* 2017; Taileb *et al.* 2018; Sow, Lau-Chapdelaine & Radulescu 2021; Taileb, Meluguizo-Gavilances & Chinnayya 2021*b*), in non-uniform mixtures (Mi, Timofeev & Higgins 2017*a*; Mi *et al.* 2017*b*), in mixtures with concentration gradients (Han, Wang & Law 2019), in mixtures with fluctuations in concentrations (Zhou *et al.* 2022), cylindrical detonation (Han *et al.* 2017), also in non-ideal configurations such as detonations bounded by an inert layer (Reynaud, Virot & Chinnayya 2017; Reynaud *et al.* 2020), with wall losses (Chinnayya, Hadjadj & Ngomo 2013; Sow *et al.* 2014; Sow, Chinnayya & Hadjadj 2015, 2019), in two-phase detonations with water spray (Watanabe *et al.* 2019, 2020, 2021) and with fuel spray (Jourdaine, Tsuboi & Hayashi 2022).

All these studies have extracted their 1-D profiles from straight lines parallel to the direction of detonation propagation. However, Sow *et al.* (2021) showed that these straight lines did not coincide with the material trajectories, due to convective mixing, which increased with lower isentropic indexes, due to jet enhancement. Moreover, Borzou (2016) and Radulescu (2018) tracked Lagrangian tracers, trajectories of which were affected by the cellular structure of a single-headed detonation. These studies are the very few previous investigations on dispersion behind a detonation front, to the best of our knowledge. In addition, the comparison between Lagrangian and Eulerian averaging processes has not been done yet.

In order to address this issue, unsteady two-dimensional (2-D) simulations with the Lagrangian particle tracking method were conducted for detonation in a straight channel for two mixtures of increased irregularity. Both the distance travelled by the Lagrangian particle behind the front and the time from shock passage were recorded in the course of the simulations. The degree of the dispersion and the relative dispersion (Babiano *et al.* 1990; Sawford 2001; Salazar & Collins 2009) were evaluated. Two new Favre average procedures, based on the distance travelled by the Lagrangian particle or the time from the shock passage were proposed to assess the accuracy of the previous Eulerian Favre average procedure.

The plan of this paper is as follows. The governing equations and the numerical method are presented in §§ 2.1 and 2.2, respectively. The procedure to record the values for each Lagrangian particle is explained in § 2.3. Section 3 describes the problem statement.

The results and discussions are given in § 4. The dispersion behind the detonation front and the anisotropic motion are firstly examined in § 4.1. Then, the dispersion in the induction time scale is analysed in § 4.2. Furthermore, the relative dispersion is discussed in § 4.3. Moreover, the two new Lagrangian Favre average procedures are described and the 1-D profiles from these procedures are compared with the Eulerian estimates in § 4.4. Finally, the main conclusions are drawn in § 5.

2. Numerical set-up

2.1. *Governing equations*

The governing equations for the gaseous phase are the 2-D reactive compressible Navier–Stokes equations, with the ideal equation of state. The chemical reaction mechanism proposed by Hong, Davidson & Hanson (2011), which considers nine species (H_2, O_2, H, O, OH, H_2O, HO_2, H_2O_2 and Ar) and 20 elemental reactions, is used. In addition, the reliable performance of this detailed chemical reaction mechanism can be achieved over a range of the reactant concentrations, stoichiometries, pressures and temperatures from 950 K to greater than 3000 K according to the validation by Hong *et al.* (2011). Here,

$$\frac{\partial \boldsymbol{U}}{\partial t}+\frac{\partial \boldsymbol{E}}{\partial x}+\frac{\partial \boldsymbol{F}}{\partial y}+\frac{\partial \boldsymbol{E_d}}{\partial x}+\frac{\partial \boldsymbol{F_d}}{\partial y}=\boldsymbol{S}, \tag{2.1}$$

$$\boldsymbol{U}=\begin{bmatrix}\rho\\ \rho u\\ \rho v\\ e\\ \rho Y_k\end{bmatrix},\quad \boldsymbol{E}=\begin{bmatrix}\rho u\\ \rho u^2+p\\ \rho uv\\ (e+p)u\\ \rho Y_k u\end{bmatrix},\quad \boldsymbol{F}=\begin{bmatrix}\rho v\\ \rho uv\\ \rho v^2+p\\ (e+p)v\\ \rho Y_k v\end{bmatrix}, \tag{2.2a–c}$$

$$\boldsymbol{E_d}=\begin{bmatrix}0\\ -\tau_{xx}\\ -\tau_{xy}\\ -\tau_{xx}u-\tau_{xy}v+q_x\\ j_{x,k}\end{bmatrix},\quad \boldsymbol{F_d}=\begin{bmatrix}0\\ -\tau_{yx}\\ -\tau_{yy}\\ -\tau_{yx}u-\tau_{yy}v+q_y\\ j_{y,k}\end{bmatrix},\quad \boldsymbol{S}=\begin{bmatrix}0\\ 0\\ 0\\ 0\\ \dot{\omega}_k\end{bmatrix}, \tag{2.3a–c}$$

$$p=\rho RT, \tag{2.4}$$

where, x, y, t, ρ, u, v, p, T, e, Y_k and $R=R_u(\sum_{k=1}^{N_s} Y_k/W_k)$ are longitudinal coordinate, transverse coordinate, time, density, velocity in x direction, velocity in y direction, pressure, temperature, total energy, mass fraction of species k and gas constant, respectively. Here N_s, R_u and W_k are the total number chemical species, universal gas constant, and molecular weight of species k. τ, q, j_k and $\dot{\omega}_k$ denote the shear stress, heat flux, diffusion flux and reaction rate, respectively. The total energy can be written as the following formula:

$$e=\sum_{k=1}^{N_s}\rho Y_k h_k-p+\tfrac{1}{2}\rho(u^2+v^2). \tag{2.5}$$

Here, h_k is enthalpy for species k. The Stokes' hypothesis is utilized and the bulk viscosity can be neglected. The shear stress is expressed as

$$\tau_{xx} = \frac{2}{3}\mu\left(2\frac{\partial u}{\partial x} - \frac{\partial v}{\partial y}\right), \tag{2.6}$$

$$\tau_{xy} = \tau_{yx} = \mu\left(\frac{\partial u}{\partial y} + \frac{\partial v}{\partial x}\right), \tag{2.7}$$

$$\tau_{yy} = \frac{2}{3}\mu\left(2\frac{\partial v}{\partial y} - \frac{\partial u}{\partial x}\right). \tag{2.8}$$

Here, μ is viscosity. The heat flux is the sum of the heat flux by the temperature gradient (i.e. Fourier's law) and the heat flux by the enthalpy transport. The heat flux caused by concentration gradients, i.e. Dufour effect, is neglected in this study because the Dufour effect is negligibly small in the combustion process (Warnatz, Maas & Dibble 2006).

$$q_x = -\kappa\frac{\partial T}{\partial x} - \rho\sum_{k=1}^{N_s} h_k D_k \frac{\partial Y_k}{\partial x}, \tag{2.9}$$

$$q_y = -\kappa\frac{\partial T}{\partial y} - \rho\sum_{k=1}^{N_s} h_k D_k \frac{\partial Y_k}{\partial y}. \tag{2.10}$$

Here, κ and D_k are thermal conductivity and diffusion coefficient for species k. The diffusive flux is evaluated using Fick's law as the following equations:

$$j_{x,k} = -\rho D_k \frac{\partial Y_k}{\partial x}, \tag{2.11}$$

$$j_{y,k} = -\rho D_k \frac{\partial Y_k}{\partial y}. \tag{2.12}$$

The diffusive flux caused by temperature gradient, i.e. Soret effect, is neglected in this study. The Soret effect is only important for light species and at low temperature (Warnatz *et al.* 2006) so that its effect will be negligible for the propagation of detonation wave and the flow field behind the front. D_k used in (2.11) and (2.12) is evaluated by the mixing rule for the diffusive flux in terms of the mass fraction (Kee, Coltrin & Glarborg 2003) (see (2.33)) so that the expression for the diffusive flux in mixture average evaluation is consistent. The correction velocity to ensure that the summation of the diffusive fluxes is zero was not taken into account in our computations. Indeed, the magnitude of correction is significantly small (Reaction Design 2000). Moreover, in order to ensure that the summation of the mass fractions to be one numerically, each mass fraction was normalized by the summation of the mass fractions, after the numerical integration.

The thermodynamic properties such as enthalpy h_k, specific heat at the constant pressure $c_{p,k}$ and entropy s_k^0 for species k are assumed to be functions of temperature and are determined from the Janaf thermochemical polynomials (McBride, Gordon & Reno 1993):

$$\frac{h_k}{(R_u/W_k)T} = a_{1,k} + \frac{a_{2,k}}{2}T + \frac{a_{3,k}}{3}T^2 + \frac{a_{4,k}}{4}T^3 + \frac{a_{5,k}}{5}T^4 + \frac{a_{6,k}}{T}, \tag{2.13}$$

$$\frac{c_{p,k}}{R_u/W_k} = a_{1,k} + a_{2,k}T + a_{3,k}T^2 + a_{4,k}T^3 + a_{5,k}T^4, \tag{2.14}$$

$$\frac{s_k^0}{R_u/W_k} = a_{1,k}\ln T + a_{2,k}T + \frac{a_{3,k}}{2}T^2 + \frac{a_{4,k}}{3}T^3 + \frac{a_{5,k}}{4}T^4 + a_{7,k}. \tag{2.15}$$

Here, $a_{1,k}$, $a_{2,k}$, $a_{3,k}$, $a_{4,k}$, $a_{5,k}$, $a_{6,k}$ and $a_{7,k}$ are the coefficients depending on the species k and temperature range ($T < 1000\,\mathrm{K}$ or $T \geqq 1000\,\mathrm{K}$).

From a preliminary study, a method proposed by Gordon, McBride & Zeleznik (1984) is shown to be accurate compared with the experimental data as for the viscosity and thermal conductivity. However, the coefficients for HO_2 in a method proposed by Gordon *et al.* (1984) are not available. As for the transport properties of viscosity μ_k and thermal conductivity κ_k for species k apart from HO_2, a method proposed by Gordon *et al.* (1984) is used to estimate the gas viscosity and thermal conductivity as the following equations:

$$\ln \mu_k = C_{1,k}^{\mu}\ln T + \frac{C_{2,k}^{\mu}}{T} + \frac{C_{3,k}^{\mu}}{T^2} + C_{4,k}^{\mu}, \tag{2.16}$$

$$\ln \kappa_k = C_{1,k}^{\kappa}\ln T + \frac{C_{2,k}^{\kappa}}{T} + \frac{C_{3,k}^{\kappa}}{T^2} + C_{4,k}^{\kappa}. \tag{2.17}$$

Here, $C_{1,k}^{\mu}$, $C_{2,k}^{\mu}$, $C_{3,k}^{\mu}$, $C_{4,k}^{\mu}$, $C_{1,k}^{\kappa}$, $C_{2,k}^{\kappa}$, $C_{3,k}^{\kappa}$ and $C_{4,k}^{\kappa}$ are the coefficients depending on the species k and temperature range ($T < 1000\,\mathrm{K}$ or $T \geqq 1000\,\mathrm{K}$).

The viscosity and thermal conductivity for HO_2 are calculated from the Chapman–Enskog method (Chapman & Cowling 1991) and the Eucken method (Poling, Prausnitz & O'Connel 2001), respectively.

The viscosity for HO_2 is evaluated by the Chapman–Enskog method (Chapman & Cowling 1991) by

$$\mu_{HO_2} = 2.6693 \times 10^{-6}\frac{\sqrt{W_{HO_2}T}}{\sigma_{HO_2}^2\Omega_{22}}. \tag{2.18}$$

Here, σ_{HO_2} and Ω_{22} are the Lennard–Jones collision diameter for HO_2 and the collision integral, respectively. The collision integrals Ω_{22} are calculated from the following empirical formula suggested by Neufeld, Janzen & Aziz (1972):

$$\Omega_{22} = C_1^{22}(T^*)^{-C_2^{22}} + C_3^{22}\exp(-C_4^{22}T^*) + C_5^{22}\exp(-C_6^{22}T^*). \tag{2.19}$$

Here, the constants in (2.19) are defined as follows: $C_1^{22} = 1.16145$; $C_2^{22} = 0.14874$; $C_3^{22} = 0.52487$; $C_4^{22} = 0.77320$; $C_5^{22} = 2.16178$; $C_6^{22} = 2.43787$. Here, T^* is the reduced temperature given by

$$T^* = \frac{k_B T}{\varepsilon_k}. \tag{2.20}$$

Here, ε_k and k_B are the Lennard–Jones potential well depth for species k and the Boltzmann constant, respectively. The thermal conductivity for HO_2 is evaluated by the Eucken method (Poling *et al.* 2001) as

$$\kappa_{HO_2} = \frac{7}{2}R_u\mu_{HO_2}. \tag{2.21}$$

The Wilke method (Wilke 1958) and the Wassiljewa method (Law 2006) are used to estimate the multicomponent gas viscosity and thermal conductivity based on the pure

species values:

$$\mu = \sum_{k=1}^{N_s} \frac{\mu_k}{1 + \dfrac{1}{X_k} \displaystyle\sum_{l \neq k}^{N_s} X_l \Phi_{kl}}, \tag{2.22}$$

$$\kappa = \sum_{k=1}^{N_s} \frac{\kappa_k}{1 + \dfrac{1.065}{X_k} \displaystyle\sum_{l \neq k}^{N_s} X_l \Phi_{kl}}. \tag{2.23}$$

Here, X_k is the molar fraction for species k and Φ_{kl} is calculated as

$$\Phi_{kl} = \frac{[1 + (\mu_k/\mu_l)^{1/2}(W_l/W_k)^{1/4}]^2}{2\sqrt{2}(1 + W_k/W_l)^{1/2}}. \tag{2.24}$$

The diffusion coefficient of a compound k into the mixture of the other compounds is evaluated based on the binary diffusion coefficient between the species k and l from the Chapman–Enskog method (Chapman & Cowling 1991). The binary diffusion coefficient between the species k and l is the function of temperature and pressure and expressed as the following formula:

$$D_{kl} = 2.628 \times 10^{-2} \frac{\sqrt{T^3}}{p\sigma_{kl}^2 \Omega_{11}} \sqrt{\frac{(W_k + W_l)}{2W_k W_l}}. \tag{2.25}$$

Here, σ_{kl} and Ω_{11} are the effective collision diameter for species k and l, and the collision integral. The collision integral Ω_{11} is estimated by the following empirical formula (Neufeld *et al.* 1972):

$$\Omega_{11} = \frac{C_1^{11}}{(T_d^*)^{C_2^{11}}} + \frac{C_3^{11}}{\exp(C_4^{11} T_d^*)} + \frac{C_5^{11}}{\exp(C_6^{11} T_d^*)} + \frac{C_7^{11}}{\exp(C_8^{11} T_d^*)}, \tag{2.26}$$

$$T_d^* = \frac{k_B T}{\varepsilon_{kl}}. \tag{2.27}$$

Here, the constants in (2.26) are defined as follows: $C_1^{11} = 1.06036$; $C_2^{11} = 0.15610$; $C_3^{11} = 0.19300$; $C_4^{11} = 0.47635$; $C_5^{11} = 1.03587$; $C_6^{11} = 1.52996$; $C_7^{11} = 1.76474$; $C_8^{11} = 3.89411$. Here ε_{kl} is the effective Lennard–Jones potential well depth for species k and l. Here σ_{kl} and ε_{kl} are estimated based on the Lennard–Jones collision diameter and Lennard–Jones potential well depth for species k and l, and the formula is different depending on whether the collision partners are polar or non-polar. For the case that the partners are either both polar or both non-polar, the equations are

$$\varepsilon_{kl} = \sqrt{\varepsilon_k \varepsilon_l}, \tag{2.28}$$

$$\sigma_{kl} = \frac{\sigma_k \sigma_l}{2}. \tag{2.29}$$

Here, ε_k, ε_l are the Lennard–Jones collision potential well depth for species k and l, respectively. Here σ_k and σ_l are the Lennard–Jones collision diameter for species k and

l, respectively. For the case for a polar molecule interacting with a non-polar molecule, the equations are

$$\varepsilon_{kl} = \xi^2 \sqrt{\varepsilon_k \varepsilon_l}, \tag{2.30}$$

$$\sigma_{kl} = \frac{\sigma_k \sigma_l}{2} \xi^{-(1/6)}, \tag{2.31}$$

$$\xi = 1 + \frac{1}{4} \alpha^*_{np} \mu^*_{pol} \sqrt{\frac{\varepsilon_{pol}}{\varepsilon_{np}}}. \tag{2.32}$$

Here, α^*_{np} and μ^*_{pol} are the reduced polarizability for the non-polar molecule and the reduced dipole moment for the polar molecule, respectively. The subscripts for *np* and *pol* in (2.32) denote the non-polar and polar molecule, respectively. The diffusion coefficient of a compound k into the mixture of the other compound D_k to estimate the diffusive flux using the mass fraction gradient is calculated by the following mixing rule (Kee *et al.* 2003):

$$D_k = \frac{1}{\displaystyle\sum_{l \neq k}^{N_s} \frac{X_l}{D_{kl}} + \frac{X_k}{1 - Y_k} \sum_{l \neq k}^{N_s} \frac{Y_k}{D_{kl}}}. \tag{2.33}$$

The trajectories of the gas particles can be simply obtained by massless Lagrangian particles with the following equations:

$$\frac{\mathrm{d}x_{p,i}}{\mathrm{d}t} = u_i, \tag{2.34}$$

$$\frac{\mathrm{d}y_{p,i}}{\mathrm{d}t} = v_i. \tag{2.35}$$

Here, $x_{p,i}$ and $y_{p,i}$ are the x position and y positions for the ith Lagrangian particle. Here u_i and v_i are the x and y components of the velocity at the ith particle position, respectively.

2.2. *Numerical methods*

The detailed formulation of the numerical method can be found in Watanabe (2020). A classical first-order operator-splitting method is employed to couple the hydrodynamics with the detail chemistry. The spatial derivatives of the convective term are discretized by a fifth-order advection upstream splitting method using pressure-based weight functions (known as AUSMPW+) improved by Kim, Kim & Rho (2001) based on a modified weighted essentially non-oscillatory scheme (known as MWENO-Z) (Hu, Wang & Chen 2016) and a second-order central differential scheme is applied to the discretization of the diffusive term. The time integration method for the convective and diffusion terms is the third-order total variation diminishing Runge–Kutta method (Gottlieb, Shu & Tadmor 2001), and the multi-time scale method (Gou *et al.* 2010) is used for the time integration of the chemical source term.

The first-order Euler method is used for the integration of the Lagrangian particles. The gas phase quantities around the ith Lagrangian particle ψ_i are estimated by interpolating the surrounding three nearby Eulerian cell values by the barycentric interpolation

(Shimura & Matsuo 2018) as follows (see (2.36)):

$$\psi_i = c_1\psi_1 + c_2\psi_2 + c_3\psi_3. \tag{2.36}$$

Here, ψ_1, ψ_2 and ψ_3 are the gas phase quantities at three Eulerian cells nearby the ith Lagrangian particle, respectively. Here c_1, c_2 and c_3 are the normalized coefficients which are estimated based on the ratio of area of the triangles to the area of the cell (Shimura & Matsuo 2018; Watanabe 2020).

2.3. *Recording the variables for each Lagrangian particle*

The variables of each Lagrangian particle were recorded during the course of their trajectories, being updated every time step. The time when the Lagrangian particles passed the leading shock front t_{shock} was recorded by the first pressure jump experienced by the Lagrangian particles to estimate the time from the shock passage $\tau = t - t_{shock}$. The dispersion of the Lagrangian particles were evaluated by the distance travelled by the Lagrangian particle after the shock passage from (2.37), (2.38) and (2.39). The equations (2.37) and (2.38) refer to the longitudinal and transverse distances travelled by the Lagrangian particle after the shock passage, respectively; equation (2.39) represents the distance travelled by the Lagrangian particle after the shock passage:

$$x_i = \int u_i \,\mathrm{d}t, \tag{2.37}$$

$$y_i = \int |v_i| \,\mathrm{d}t, \tag{2.38}$$

$$x_{xy,i} = \int (u_i^2 + v_i^2)^{1/2} \mathrm{d}t. \tag{2.39}$$

Tracking of the Lagrangian particles enabled us to obtain the time when the induction process was completed. The thermicity $\dot{\sigma}$, which denotes the influence of chemical reaction on the flow velocity due to both chemical energy release and change in the number of moles present, was used to define the induction time. The thermicity was defined by the following equation and calculated based on the variables at each Lagrangian particle position:

$$\dot{\sigma} = \sum_{k=1}^{N_s} \left(\frac{W}{W_k} - \frac{h_k}{c_p T} \right) \frac{\dot{\omega}_k}{\rho}. \tag{2.40}$$

During the simulation, the time, the x- and y- Lagrangian particle positions and the distance travelled by the Lagrangian particle when the thermicity was maximum were recorded and updated every time step. The induction time was defined as the time from the shock front to the time when the thermicity was maximum in this study. With the use of the Lagrangian particle tracking method, the induction time for each Lagrangian particle can be accurately evaluated from the difference between the time when the Lagrangian particle passed the leading shock front and the time when the thermicity was maximum.

3. Problem statement

The schematics for the computational target is shown in figure 1(*a*). The fully developed 2-D gaseous detonation propagates in a straight channel. Two types of reactive

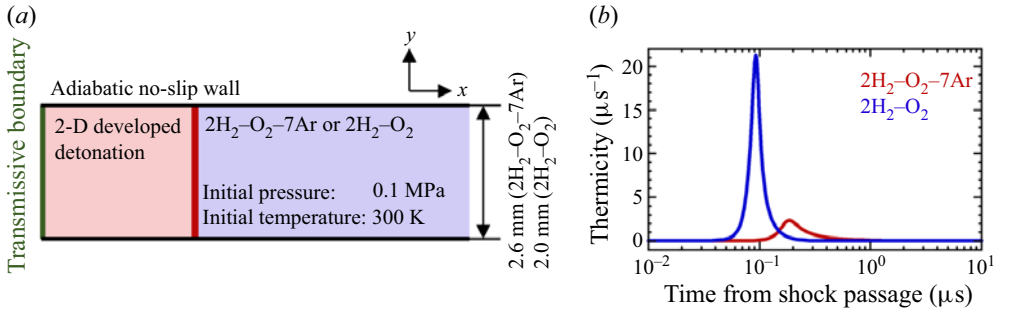

Figure 1. Simulation set-up. (*a*) Schematics of the computational target. (*b*) The ZND thermicity profile in $2H_2$–O_2–7Ar and $2H_2$–O_2 mixtures.

Parameters	$2H_2$–O_2–7Ar	$2H_2$–O_2
D_{CJ} (m s^{-1})	1690.7	2834.3
M_{CJ}	4.8	5.3
x_{ind} (μm)	76.6	48.6
x_{reac} (μm)	409	72.5
τ_{ind} (μs)	0.2	0.09
τ_{reac} (μs)	0.1	0.02
$E_a/(RT_{vN})$	4.1	6.9
χ	0.8	4.6
γ_{vN}	1.49	1.32

Table 1. Parameters of the reactive mixtures in the present conditions.

mixtures have been investigated: 70 % diluted stoichiometric hydrogen oxygen mixture $2H_2$–O_2–7Ar and stoichiometric hydrogen oxygen mixture $2H_2$–O_2 at ambient conditions (0.1 MPa and 300 K). The effect of instabilities can thus be assessed on the dispersion and the averaging processes. Figure 1(*b*) shows the thermicity profile for both mixtures. Table 1 lists the various parameters for both mixtures characterizing detonation such as the CJ velocity D_{CJ}, the CJ Mach number M_{CJ}, the induction length x_{ind}, the reaction length x_{reac}, the induction time τ_{ind}, the reaction time τ_{reac}, the reduced activation energy $E_a/(RT_{vN})$, the $\chi = (E_a/(RT_{vN}))(x_{ind}/x_{reac})$ parameter, and the specific heat ratio at von Neumann (vN) state γ_{vN}. Following the definition by Radulescu (2003) and Ng *et al.* (2005*b*), the induction length x_{ind} was defined as the distance from the leading shock front to the position where the thermicity was maximum, and the reaction length x_{reac} was estimated by $u_{CJ}/\dot{\sigma}_{max}$ using the maximum thermicity $\dot{\sigma}_{max}$ and the velocity at the CJ plane in the shock frame u_{CJ}. In addition, the induction time τ_{ind} was estimated from the time from the leading shock front to the time when thermicity was maximum, and the reaction time τ_{reac} was defined as the half-pulse-width time of thermicity, respectively. The induction time for the $2H_2$–O_2 mixture is approximately two times shorter than that for the $2H_2$–O_2–7Ar mixture and the peak thermicity for $2H_2$–O_2 is approximately one order of magnitude higher compared with that for the $2H_2$–O_2–7Ar mixture in the present conditions (figure 1*b* and table 1). The mixtures can be classified as weakly and mildly unstable mixtures, according to the stability analysis (Eckett, Quirk & Shepherd 2000; Austin *et al.* 2005) based on the reduced activation energy and CJ Mach number. Based on the χ parameter and CJ Mach number, the instability parameters lie slightly below and above the neutral stability curve, for the diluted and non-diluted cases (Ng *et al.* 2005*b*).

The channel widths for $2H_2$–O_2–7Ar and $2H_2$–O_2 mixtures are 2.6 and 2.0 mm, respectively. The boundary condition for the walls is the adiabatic non-slip wall and the transmissive boundary is applied to the left end. The grid is uniform and the grid width is equal at 2.0 and 1.6 μm from the region from the shock front up to 20.6 and 11.5 mm behind the front for the $2H_2$–O_2–7Ar mixture and $2H_2$–O_2 mixture, respectively. The computational domain with the minimum grid width encompassed the mean leading shock front and the mean sonic plane, which were evaluated in § 4.4. Then, the grid is stretched. The grid resolution is approximately 38 and 30 points per CJ induction length for the $2H_2$–O_2–7Ar mixture and the $2H_2$–O_2 mixture, respectively. This resolution has been shown to be largely sufficient to capture the mean structure (Reynaud *et al.* 2017, 2020). In addition, this resolution is enough to reproduce the features of the instantaneous flow fields for weakly unstable mixtures (Mazaheri, Mahmoudi & Radulescu 2012). The grid resolution study was performed in Appendix A and the main conclusions were not called into question by the present grid resolution. For more highly unstable mixtures, this resolution may not be sufficient to capture the unsteady burning mechanism of the unburnt pockets that are likely to form downstream of the leading shocks. The Courant–Friedrichs–Lewy number was fixed at 0.2 and the typical time step size was around 1.0×10^{-10} and 0.5×10^{-10} s for $2H_2$–O_2–7Ar and $2H_2$–O_2 mixtures, respectively.

The recycling block technique (Sow *et al.* 2019) is applied to enable the detonation to propagate a distance long enough to obtain statistical values. When the leading shock front reached the right-hand boundary during the simulations, the new region with the upstream condition for unburned state was appended to the right of the computational domain and the region near the left-hand boundary which was far from the mean sonic plane was discarded. The same procedure was also applied for the Lagrangian particles. When the leading shock front reached the right-hand boundary during the simulations, the new Lagrangian particles were located to the right of the computational domain and the Lagrangian particles which were located in the discarded left-hand domain were excluded from the simulations. The recycling block technique was successfully utilized to reduce the computational cost by the use of smaller computational domain and to simulate the detonation propagation in the previous studies (Reynaud *et al.* 2017, 2020; Sow *et al.* 2019; Watanabe *et al.* 2020, 2021; Taileb, Meluguizo-Gavilances & Chinnayya 2021*a*; Taileb *et al.* 2021*b*). The length of the propagation for the average procedure is approximately 1000 x_{ind} for $2H_2$–O_2–7Ar and 1200 x_{ind} for $2H_2$–O_2. This study has cost approximately 2.0×10^6 CPU hours with 64 processors.

The Lagrangian particles are initially located in the fresh mixture in every grid point. The number of these particles inside the computational domain changes during the simulation due to the recycling block method and are around 34×10^6 and 25×10^6 for the $2H_2$–O_2–7Ar mixture and the $2H_2$–O_2 mixture, respectively. In order to get the averaged values, the instantaneous 2-D flow fields are saved each time the detonation front propagates 0.5 x_{ind}. The total number of the particles in the region where the detonation propagates is approximately 5×10^7 and 6×10^7 for the $2H_2$–O_2–7Ar and $2H_2$–O_2 mixtures, respectively.

4. Results and discussions

4.1. *Dispersion and anisotropy*

Firstly, the global features of the $2H_2$–O_2–7Ar and $2H_2$–O_2 mixtures are depicted using the instantaneous 2-D flow fields in figures 2 and 3, respectively. In the $2H_2$–O_2–7Ar

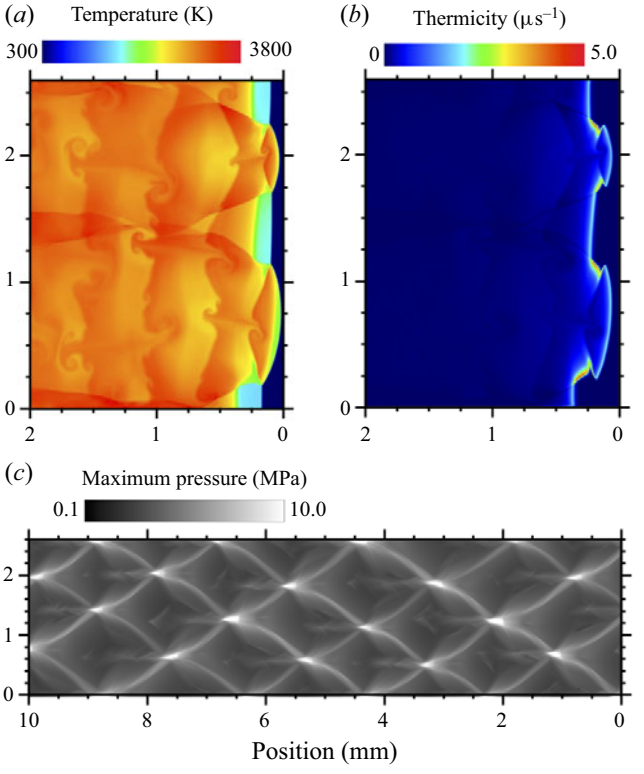

Figure 2. The 2-D instantaneous flow fields in $2H_2$–O_2–7Ar mixture: (*a*) temperature; (*b*) thermicity; (*c*) maximum pressure.

mixture, the cellular structure is regular with two cells in the channel (figure 2*c*). No unburned gas pocket is formed behind the front and the classical key stone feature can be observed (figure 2*a*,*b*). As for the $2H_2$–O_2 mixture, the cellular structure and the frontal shape were more irregular (figure 3), expected from the increased instability parameters. The unburned gas pockets are torn apart from the front and continue to burn downstream (figure 3*a*,*b*). In both cases, strong transverse wave structures occurred in the second part of the cell (figures 2*b* and 3*b*), as also observed experimentally by Desbordes & Presles (2012). The thermicity fields indicated that the heat release took place much more rapidly and sometimes one order of magnitude quicker in the non-diluted case than in the diluted case (figures 2*b* and 3*b*). The average propagation velocity for both mixtures agreed with that of the CJ velocity. The average cell width in the simulations from the manual measurement of 150 and 300 cells for the $2H_2$–O_2–7Ar and $2H_2$–O_2 mixtures is 1.3 and 0.7 mm, respectively. The experimental cell width for the $2H_2$–O_2–7Ar mixture is expected to be 2.7–4.0 mm from similar mixture conditions, and the cell width reported from experiments for the $2H_2$–O_2 mixture ranges from 1.4 to 2.1 mm (Kaneshige & Shepherd 1997). Therefore, the cell sizes in the simulations were thus smaller that the experimental ones by a factor of approximately 2–3. The numerical cell width is reported to be smaller as in previous studies (Taylor *et al.* 2013; Taileb *et al.* 2021*a*). This is not due to the present numerical resolution but may be due to vibrational non-equilibrium effects (Taylor *et al.* 2013; Shi *et al.* 2017), uncertainties of the chemical reaction model in

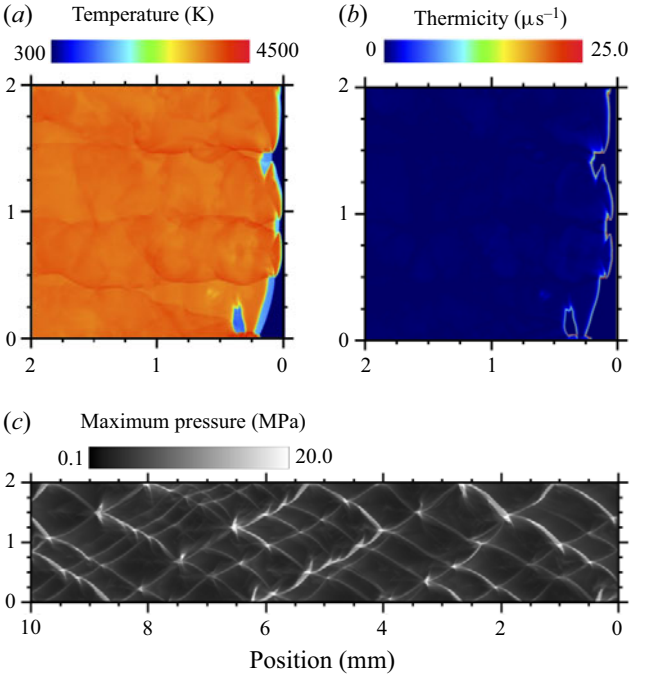

Figure 3. The 2-D instantaneous flow fields in $2H_2$–O_2 mixture: (*a*) temperature; (*b*) thermicity, (*c*) maximum pressure.

detonation conditions (Mével & Gallier 2018) and three-dimensional (3-D) effects (Taileb *et al.* 2018; Monnier *et al.* 2022; Crane *et al.* 2023).

Figures 4 and 5 show the instantaneous 2-D flow fields in the Lagrangian perspective for (*a*) time front shock passage; (*b*) longitudinal distance travelled by the particle x_i; (*c*) transverse distance travelled by the particle y_i; (*d*) distance travelled by the particle $x_{xy,i}$ from shock passage for the $2H_2$–O_2–7Ar and $2H_2$–O_2 mixtures, respectively. As we move away from the leading shocks, the time from shock passage and the longitudinal distance x_i increased. However, their distributions were not uniform in each section, regardless of the mixture instability. This non-uniform distribution of the Lagrangian particles is consistent with the numerical findings of Sow *et al.* (2021). The scales of the legends for figures 4(*a*) and 5(*a*) are different, due to the difference in detonation velocities for both mixtures. It can also be seen that x_i and $x_{xy,i}$ were almost the same, due to the fact that y_i remained one order of magnitude lower. In the rest of the paper, only the field of x_i will be discussed instead of that of $x_{xy,i}$. More noticeable was that the transverse distance y_i was much spottier for the non-diluted case, as we moved away from the leading shocks, indicative of more vortical structures. Large tongues of gas were also seen to penetrate the different layers and to be entrained in the x-direction. The longitudinal distance x_i for the particles inside the boundary layer can also be seen to be shorter than that of the other particles in the core of the flow.

In order to compare the distribution of the distances for both mixtures, the average longitudinal distance $\bar{x}_i$ is shown in figure 6. The slopes are different due to the difference in the velocity induced by detonation of both mixtures. The standard deviation for x_i (see figure 7*a*) $[\sum_i^N (x_i - \bar{x}_i)^2/N]^{1/2}$ were almost the same. The average transverse distance $\bar{y}_i$

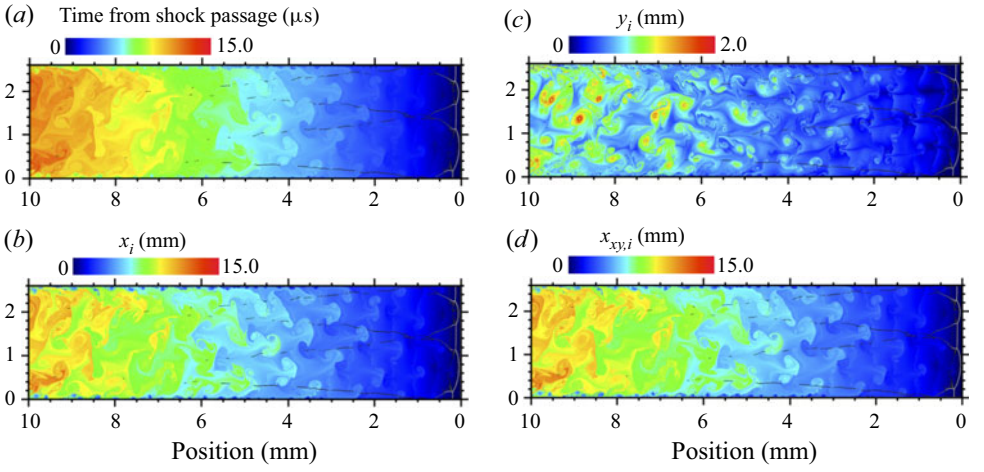

Figure 4. The 2-D instantaneous Lagrangian flow fields in $2H_2$–O_2–7Ar mixture, superimposed with Schlieren density: (*a*) time from shock passage; (*b*) longitudinal distance travelled by the Lagrangian particle x_i; (*c*) transverse distance travelled by the Lagrangian particle y_i; (*d*) distance travelled by the Lagrangian particle $x_{xy,i}$.

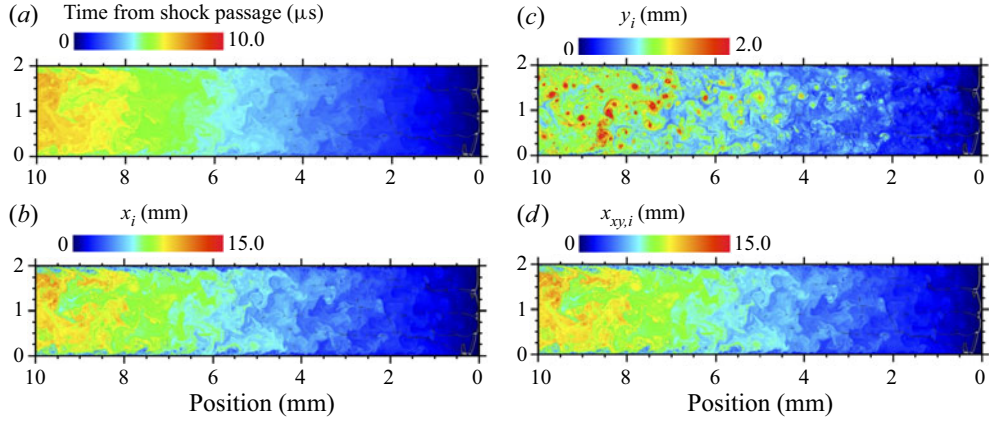

Figure 5. The 2-D instantaneous Lagrangian flow fields in $2H_2$–O_2 mixture, superimposed with Schlieren density: (*a*) time from shock passage; (*b*) longitudinal distance travelled by the Lagrangian particle x_i; (*c*) transverse distance travelled by the Lagrangian particle y_i; (*d*) distance travelled by the Lagrangian particle $x_{xy,i}$.

(see figure 7*b*) can be as high as twice for the non-diluted as compared with the more stable case.

Figures 8(*a*,*b*) and 9(*a*,*b*) depict the joint probability density function (p.d.f.) between the times from shock passage and the longitudinal and transverse distances travelled by the particles. The width of the distributions became wider as the time from the shock passage increased. The fluctuations along the transverse distance y_i also increased (see figures 8*d* and 9*d*). From figures 8(*c*,*d*) and 9(*c*,*d*), the peak of the p.d.f. for the fluctuations along the longitudinal direction was lower than that of the transverse direction, meaning that the dispersion along the longitudinal direction was greater than that of the transverse one. This finding that the dispersion along the longitudinal direction was greater than that of

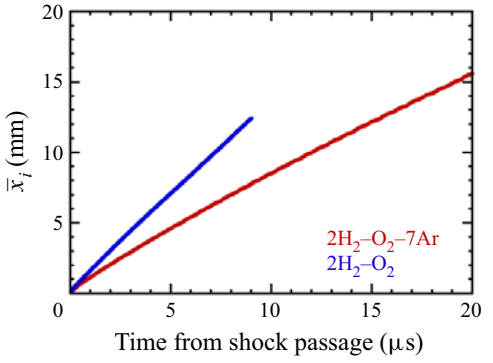

Figure 6. Average longitudinal distance $\bar{x}_i$ for $2H_2$–O_2–7Ar and $2H_2$–O_2 mixtures.

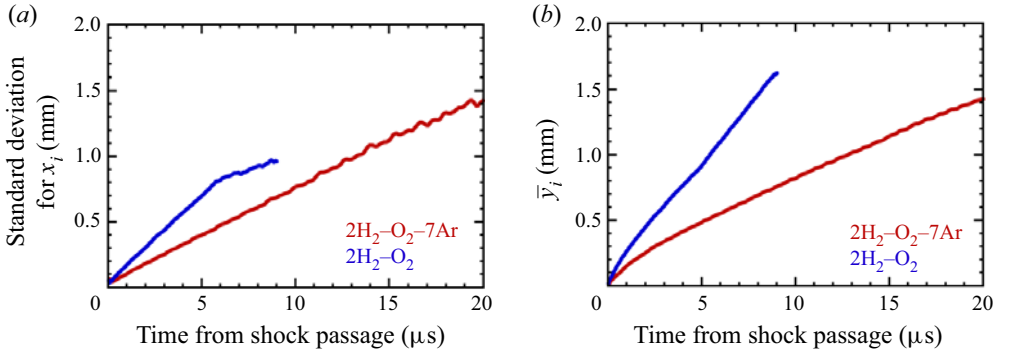

Figure 7. (*a*) Standard deviation for the longitudinal distance $[\sum_i^N (x_i - \bar{x}_i)^2/N]^{1/2}$ and (*b*) average transverse distance $\bar{y}_i$ for $2H_2$–O_2–7Ar and $2H_2$–O_2 mixtures.

the transverse wave was not what could be expected from the presence of the transverse waves, characteristics and cornerstones of the detonation cellular structure. Moreover, the comparison of figures 8(*c*,*d*) and 9(*c*,*d*) showed that the diluted case needed approximately five times more time to obtain the same level of dispersion than the non-diluted one. Indeed, the average transverse distance $\overline{y_i}$ became approximately one cell width after 17.8 μs for the argon diluted case as compared with 3.6 μs for the other case (figure 7*b*).

The 2-D instantaneous Lagrangian flow fields of the normalized fluctuations in the longitudinal distance ($\delta x_i = (x_i - \bar{x}_i)/x_i$) and the normalized transverse distance y_i/x_i have been plotted in figures 10 and 11 for both cases. Near the front, they came mainly from three factors. At first, the triple point collision resulted in forward jets with positive δx_i and in backward jets with negative values. Second, the decaying incident shock in the second part of the cell induced negative values. Finally, the transverse waves and the vortical motions played a major role in increasing y_i, the more important contribution coming from the latter, as time passed. Some differences were also present for δx_i near the boundary layer. The fluctuations appeared spottier in the more unstable non-diluted case, with vortical motions also playing a stronger role in the unstable case.

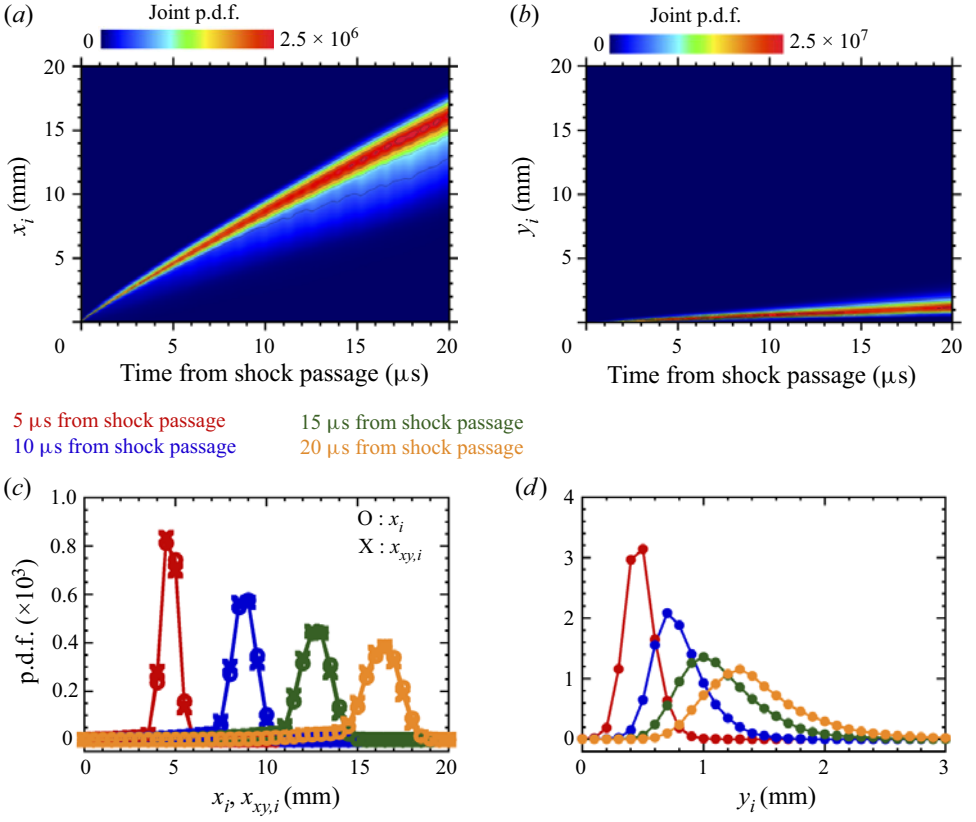

Figure 8. The $2H_2$–O_2–7Ar mixture. Joint p.d.f. between (*a*) times from shock passage and longitudinal distances x_i, (*b*) times from shock passage and transverse distances y_i. The p.d.f. at different instants for (*c*) longitudinal distances x_i and distances $x_{xy,i}$, (*d*) transverse distances y_i.

Figure 12 shows the time history of the variances of the x- and y- displacements $\overline{x_i'^2}$ and $\overline{y_i'^2}$, as well as their correlation $\overline{x_i'y_i'}$, which can be evaluated by

$$\overline{x_i'^2} = \frac{1}{N}\sum_{i=1}^{N}\left[(x_{p,i} - x_{p,i,0}) - \overline{(x_{p,i} - x_{p,i,0})}\right]^2 = \frac{1}{N}\sum_{i=1}^{N}(x_i - \overline{x_i})^2\,, \tag{4.1}$$

$$\overline{y_i'^2} = \frac{1}{N}\sum_{i=1}^{N}(y_{p,i} - y_{p,i,0})^2, \tag{4.2}$$

$$\overline{x_i'y_i'} = \frac{1}{N}\sum_{i=1}^{N}\left[(x_{p,i} - x_{p,i,0}) - \overline{(x_{p,i} - x_{p,i,0})}\right](y_{p,i} - y_{p,i,0}). \tag{4.3}$$

Here, $x_{p,i,0}$ and $y_{p,i,0}$ are x and y initial positions of the particle i, and N is the number of particles.

The levels of fluctuations of the displacements $\overline{x_i'^2}$ and $\overline{y_i'^2}$ were much higher, approximately twice in the more irregular case (see figure 12*a*). As shown previously, the fluctuations in x_i and y_i increased as we move away from the shock (figures 10

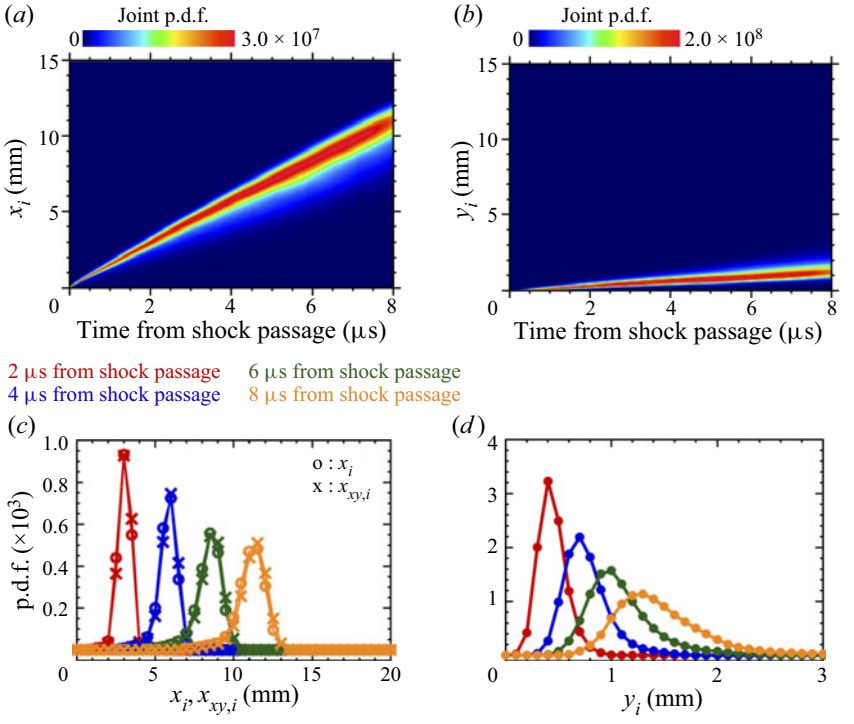

Figure 9. The $2H_2$–O_2 mixture. Joint p.d.f. between (*a*) times from shock passage and longitudinal distances x_i, (*b*) times from shock passage and transverse distances y_i. The p.d.f. at different instants for (*c*) longitudinal distances x_i and distances $x_{xy,i}$, (*d*) transverse distances y_i.

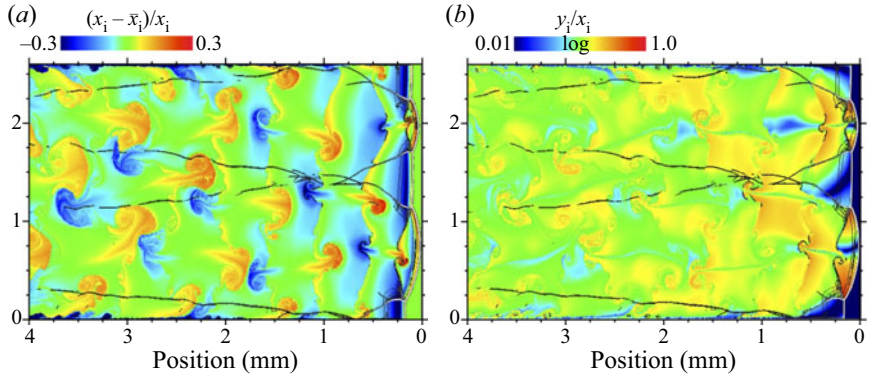

Figure 10. Diluted $2H_2$–O_2–7Ar mixture. The 2-D instantaneous Lagrangian flow fields, superimposed with Schlieren density in diluted $2H_2$–O_2–7Ar mixture. (*a*) Normalized fluctuations of the longitudinal distances $(x_i - \bar{x}_i)/x_i$. (*b*) Normalized transverse distance y_i/x_i.

and 11). The cross-relation $\overline{x_i' y_i'}$ oscillated around zero (see figure 12*c*). Indeed, the leading shock is curved and thus, for some positive y-displacements at some locations, there will be corresponding negative y-displacements at other locations. Moreover, in 2-D, for each vortex rotating clockwise, there is another vortex rotating anticlockwise. Near the leading shock, the fluctuations of transverse displacements were approximately that of the

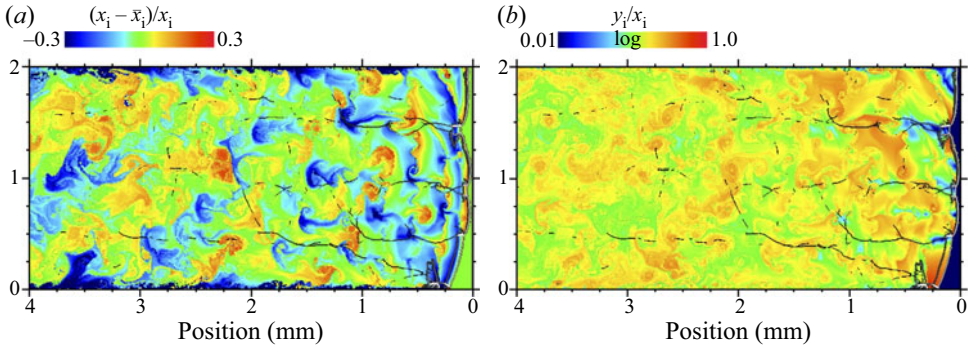

Figure 11. Non-diluted $2H_2$–O_2 mixture. The 2-D instantaneous Lagrangian flow fields, superimposed with Schlieren density in diluted $2H_2$–O_2–7Ar mixture. (*a*) Normalized fluctuations of the longitudinal distances $(x_i - \bar{x}_i)/x_i$. (*b*) Normalized transverse distance y_i/x_i.

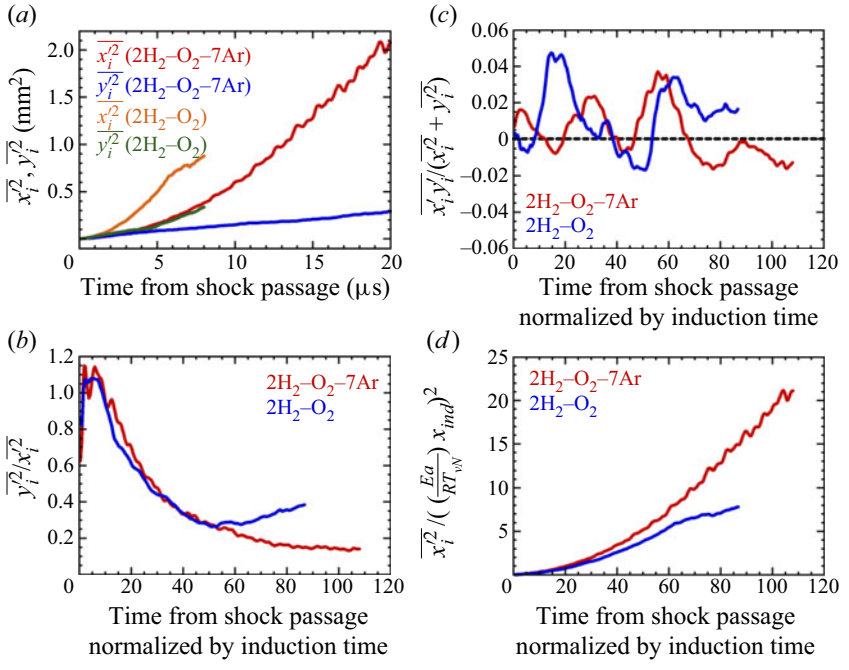

Figure 12. (*a*) Time history of the variance of the *x*- and *y*- displacements, $\overline{x_i'^2}$ and $\overline{y_i'^2}$; (*b*) non-dimensionalized *y*- displacements, $\overline{y_i'^2}/\overline{x_i'^2}$ as a function of the non-dimensionalized time τ/τ_{ind}; (*c*) $\overline{x_i'y_i'}/(\overline{x_i'^2} + \overline{y_i'^2})$; (*d*) non-dimensionalized *x*- displacements, $\overline{x_i'^2}/(E_a/(RT_{vN})x_{ind})^2$ as a function of the non-dimensionalized time τ/τ_{ind}.

longitudinal ones (see figure 12*b*). Then the *y*-levels decreased comparatively. Thus, far from the shock, the flow became anisotropic. The further evaluation of anisotropy can be found in Appendix B. In the 2-D flows investigated, there lacks the vorticity stretching mechanism that would help to return more rapidly to isotropy (see Taileb 2020). The good collapse of the curves in figure 12(*d*) suggested that a characteristic time scale was the induction time τ_{ind} and that a characteristic length scale was the induction length times the reduced activation energy $(E_a/(RT_{vN}))x_{ind}$. This scaling used for the fluctuations

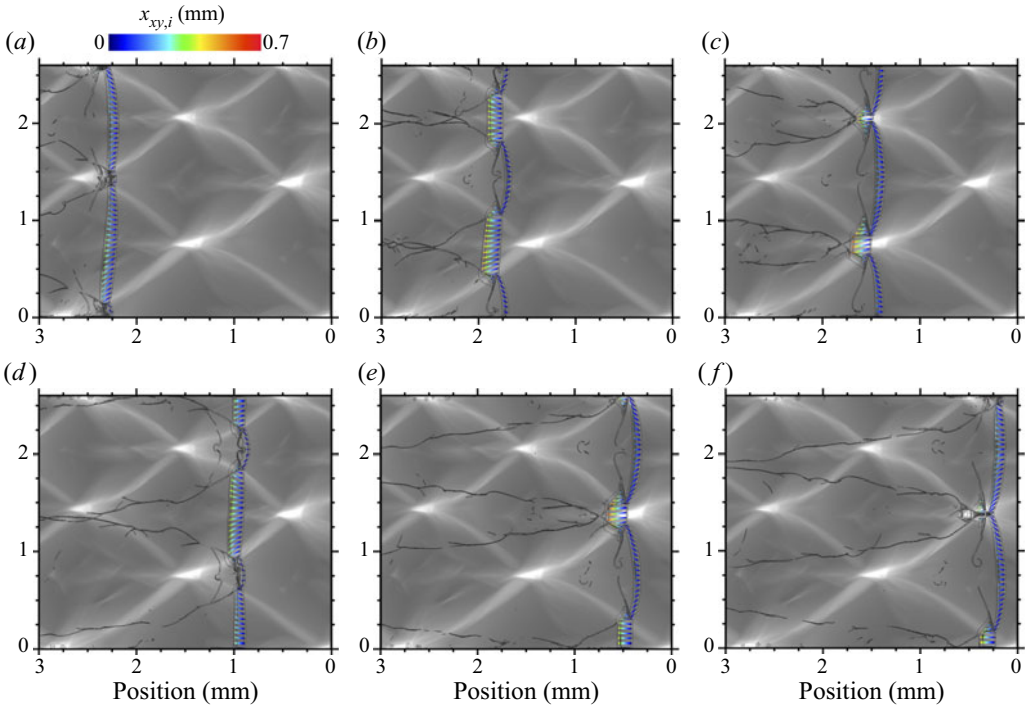

Figure 13. Time sequence of instantaneous 2-D flow fields of distance travelled from shock passage $x_{xy,i}$ in $2H_2$–O_2–7Ar mixture. Only the Lagrangian particles whose time from shock passage is less than the induction time are displayed. The Lagrangian particles selected for the display were separated by an initial vertical distance of 50 μm. The lines are the density Schlieren and the grey contour in the background is the maximum pressure. The detonation propagated from the left to the right and the time passed from (*a*) to (*f*).

of *x*-displacement as a function of the time from the shock passage is consistent with asymptotic studies (Buckmaster 1989; Lee 2008; Faria 2014) even if the same characteristic length seemed to hold also for the transverse fluctuations in the present study.

4.2. *Dispersion in induction time scale*

The dispersion was studied in this subsection within the induction time scale and was related to the cellular structure.

The time sequence of the dispersion in terms of the distance travelled by the Lagrangian particle from shock passage for $2H_2$–O_2–7Ar and $2H_2$–O_2 mixtures are depicted in figures 13 and 14, respectively. Only the Lagrangian particles whose time from shock passage is less than the induction time are displayed. When the induction time was longer, the distance travelled $x_{xy,i}$ which is only shown within the induction time scale was longer.

In the $2H_2$–O_2–7Ar mixture, the first observation is that the induction process was completed within first half of one cell cycle (figure 13). The induction length was shorter behind the Mach stem in the first part of the cell and longer behind the decaying incident shock front in the second part of the cell. After the collision of the transverse waves, the Lagrangian particles, which passed the weaker incident shock completed the induction process. The dispersion was slightly deviated from the straight line parallel to the propagation direction due to the curved leading shock front (Mölder 2016).

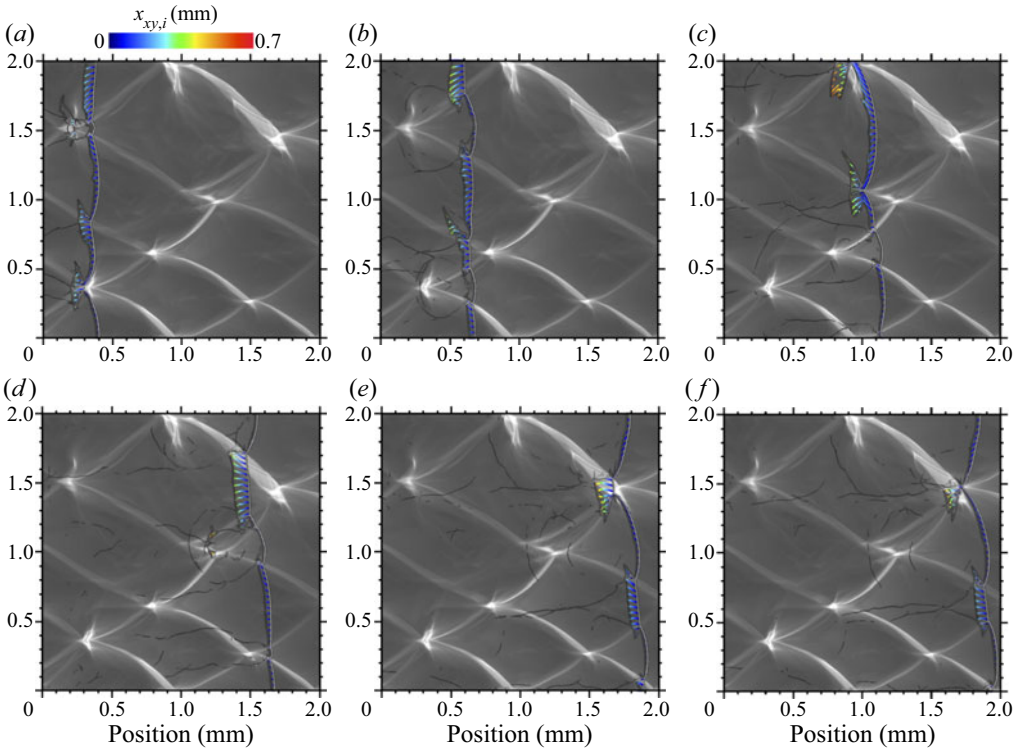

Figure 14. Time sequence of instantaneous 2-D flow fields of distance travelled from shock passage $x_{xy,i}$ in $2H_2$–O_2 mixture. Only the Lagrangian particles whose time from shock passage is less than the induction time are displayed. The Lagrangian particles selected for the display were separated by an initial vertical distance of 40 μm. The lines are the density Schlieren and the grey contour in the background is the maximum pressure. The detonation propagated from the left to the right and the time passed from (*a*) to (*f*).

In the $2H_2$–O_2 mixture, more variation in the induction time behind the leading shock front was observed due to higher reduced activation energy (figure 14). The distance in the unburned gas pocket torn from the front was also much longer (see figure 14*c*,*e*). The leading shock curvatures were also higher, inducing more deviation.

In both cases, within the induction time scale, the transverse dispersion was mainly due to the curvature of the leading shock. This effect was more pronounced near the edges of the cell and during the first part of the cell, when the leading detonation front was a Mach stem.

To relate the dispersion with the geometry of the cellular structure, the distance travelled by the Lagrangian particle and the normalized number density of Lagrangian particles α_L were shown in the position where they recorded their maximum thermicity (see figures 15 and 16). Note that the number density was the projection of Lagrangian data over the Eulerian grid, with a spacing five times greater than the minimum grid width. The number density was then normalized by its initial value at its initial position to obtain α_L,

$$\alpha_L = \frac{N_i}{N_{i,0}}, \tag{4.4}$$

where N_i and $N_{i,0}$ are the number of the Lagrangian particles, which are located on the Eulerian grid used for the projection and the number of the Lagrangian particles in the initial condition, respectively. The estimation of other variables on the Eulerian grid, such

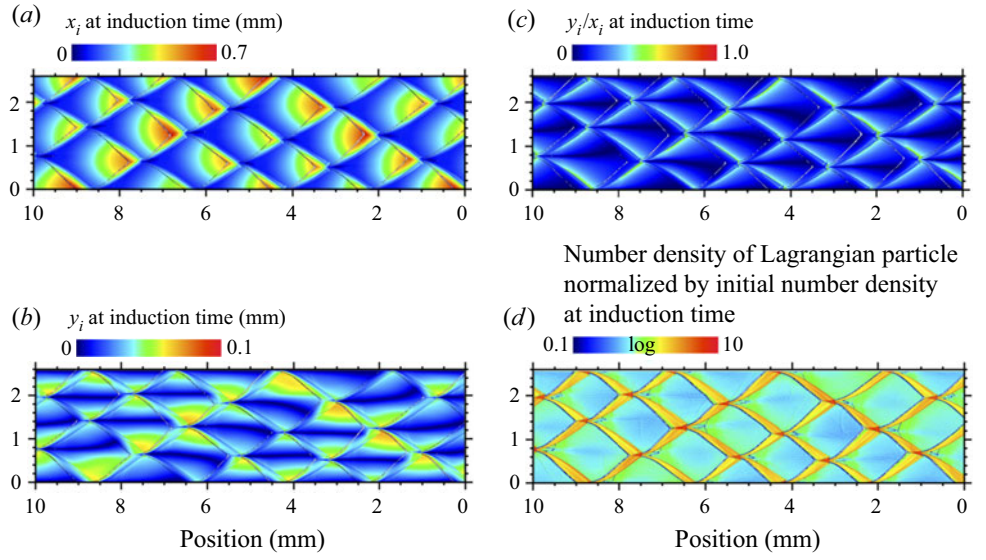

Figure 15. The 2-D flow fields of the projected Lagrangian values in the position where the Lagrangian particles experienced the maximum thermicity in $2H_2$–O_2–7Ar mixture. (*a*) Projected longitudinal distance travelled x_i at the induction time; (*b*) projected transverse distance travelled $y_{x,i}$ at the induction time; (*c*) ratio of transverse distance to longitudinal distance y_i/x_i at induction time; (*d*) number density of Lagrangian particles normalized by the initial number density. The displayed region is the same as in figure 2(*c*). The region where no Lagrangian particle was located was displayed as white colour.

as the distance travelled by Lagrangian particles, was done by the same projection over a box of width five times the grid cell size (see (4.5)),

$$\overline{\Phi_L} = \frac{\sum_{k=1}^{N_i} \Phi_{L,k}}{N_i}. \tag{4.5}$$

Here, $\overline{\Phi_L}$ and $\Phi_{L,k}$ are the projected Lagrangian value and the Lagrangian value for the kth Lagrangian particle, which were located on the Eulerian grid, respectively. The distributions of the distance travelled by Lagrangian particle and the number density at the induction time can be seen to be closely related to the cellular structure (see figures 15, 16, 2*c*, 3*c*). There are regions in the cellular structure where the Lagrangian particles did not complete the induction process (figures 15, 16). From the instantaneous flow fields, these regions were seen to be thin non-reactive tails in the gas between the leading shock front and the transverse waves due to the lower temperature, which were reported numerically by Gamezo *et al.* (2000) and observed experimentally by Xiao & Radulescu (2020) in a hydrogen–oxygen–argon mixture.

The longitudinal distance x_i tended to be larger at the end of the cell (figures 15*a*, 16*a*), due to the decaying shock wave. Near the edge of the cells, the transverse distance y_i was comparable to the longitudinal distance travelled x_i, due to the transverse waves (figures 15*b*, 16*b*). The ratio y_i/x_i was also the highest near edges (figures 15*c*, 16*c*), and increased as the mixture became more unstable. This ratio was also minimum at the centreline of the cell.

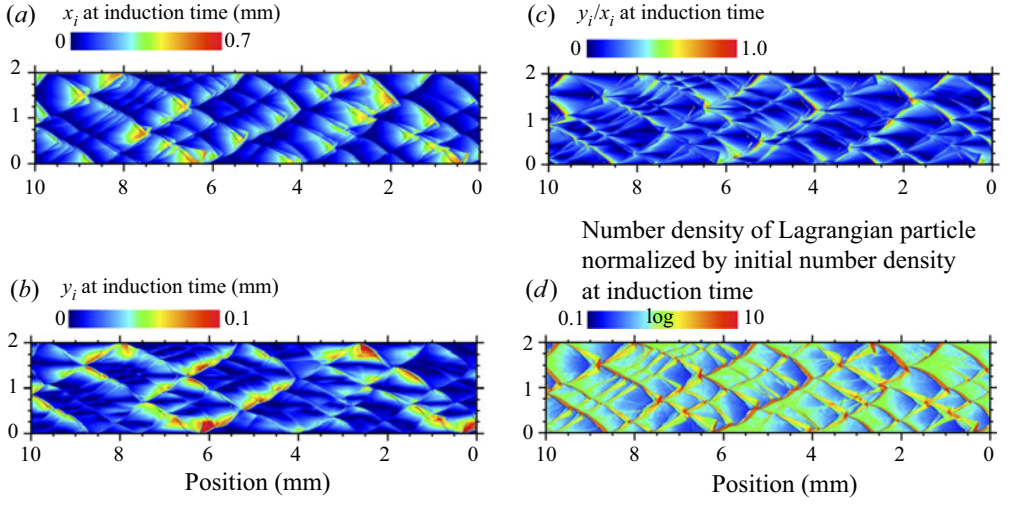

Figure 16. The 2-D flow fields of the projected Lagrangian values in the position where the Lagrangian particles experienced the maximum thermicity in $2H_2$–O_2 mixture. (*a*) Projected longitudinal distance travelled x_i at the induction time; (*b*) projected transverse distance travelled y_i at the induction time; (*c*) ratio of transverse distance to longitudinal distance y_i/x_i at induction time, (*d*) number density of Lagrangian particles normalized by the initial number density. The displayed region is the same as in figure 3(*c*). The region where no Lagrangian particle was located was displayed as white colour.

The propagation of the cellular detonation dispersed the Lagrangian particles and their distribution was non-uniform (figures 15*d*, 16*d*). The Lagrangian particles were locally accumulated the trajectory of the triple points. Fewer Lagrangian particles were found inside the cells.

In the weakly unstable $2H_2$–O_2–7Ar mixture, the number density of Lagrangian particles was the highest between the collision of the transverse waves and the triple point collision. The accumulation of Lagrangian particles at the collision point of the transverse waves gave birth to the local explosion, which induced blast waves driving the cellular structure, as modelled by Vasilev & Nikolaev (1978) and Crane *et al.* (2021).

In addition, there were some differences in the simulation results. The transverse waves accumulated the Lagrangian particles along the triple point trajectory and the other particles completed the induction process inside the cell in the simulation. This observation was in line with the previous analysis by Strehlow (1970) that the major source of the energy that produced the blast wave came from the transverse shock waves. As the mixture instability increased, the contribution of the transverse waves in the accumulation of the Lagrangian particles experiencing the maximum thermicity increased (figures 15*d*, 16*d*). In the $2H_2$–O_2 mixture, some of the strong transverse waves accumulated the particles along the triple point trajectories at the same level as near the transverse wave collision. In addition, the normalized number density can become locally higher as compared with the highest values of the diluted case.

The differences between the physical picture of the model (Vasilev & Nikolaev 1978; Crane *et al.* 2021) and the simulation results were more apparent in the $2H_2$–O_2 mixture than in the $2H_2$–O_2–7Ar mixture. These additional features on the accumulation and the dispersion of the Lagrangian particles in the induction time scale revealed in this study can provide guidelines for the development of a model for the prediction of the cellular structure and their size.

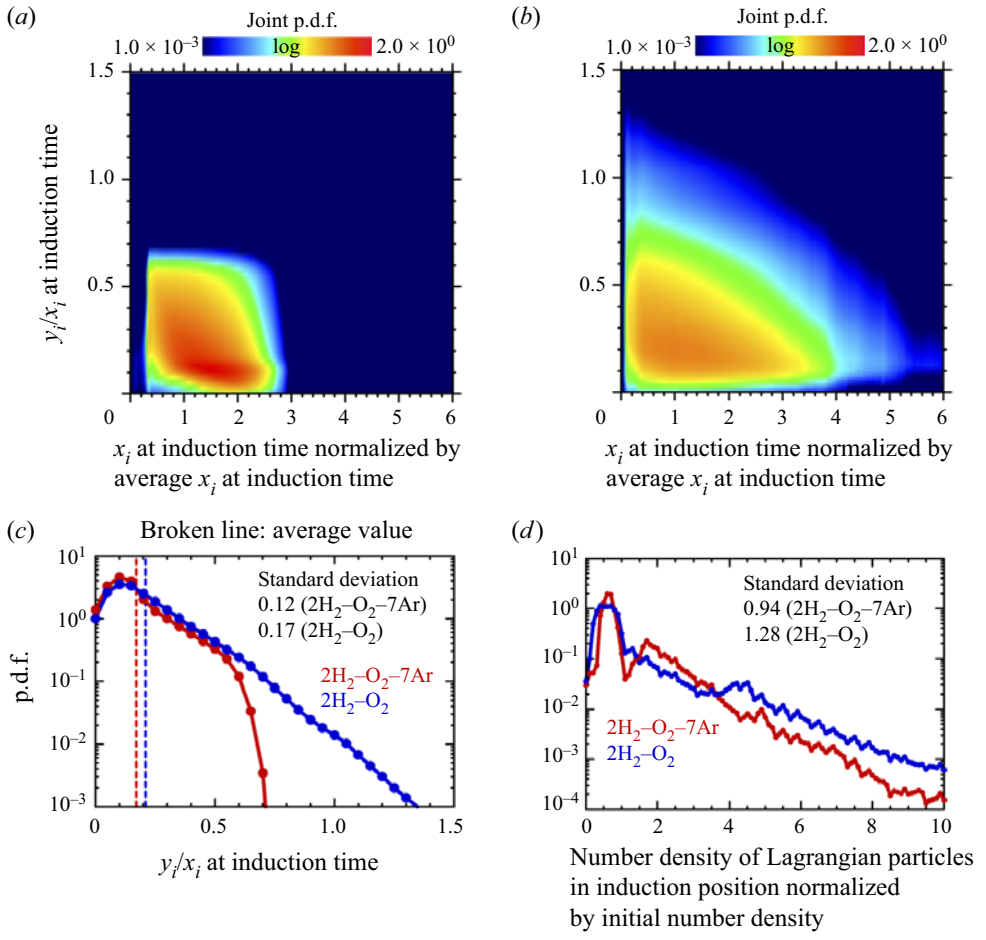

Figure 17. The p.d.f. for the values at the induction time. (*a*) Joint p.d.f. between normalized $x_i/\hat{x}_i$ and y_i/x_i in $2H_2$–O_2–7Ar mixture; (*b*) joint p.d.f. between normalized $x_i/\hat{x}_i$ and y_i/x_i in $2H_2$–O_2 mixture; (*c*) p.d.f. for y_i/x_i; (*d*) p.d.f. for normalized number density. $\hat{x}_i$ is the average of x_i at induction time over the whole computational domain.

The p.d.f. for the values at the induction time were depicted in figure 17. The distribution of normalized x_i at the induction time became wider as the mixture instability increased due to the variation of the induction time behind the cellular detonation front by the higher reduced activation energy and the presence of unburned gas pockets (figure 17*a*,*b*). The distribution of y_i/x_i was also wider and its average value was larger for the non-diluted mixture, due to stronger transverse waves (figure 17*a*–*c*). High values of y_i/x_i with small x_i could be found around the triple point trajectories, due to stronger transverse motion by stronger transverse waves (figures 15*c*, 16*c*, 17*a*,*b*). As x_i increased, y_i/x_i decreased (see figures 12*b*, 17*a*,*b*).

The peak for distribution of y_i/x_i at the induction time was located around 0.1 (figure 17*c*) and the deviation of the trajectories of particles from the straight line in the induction time scale was not large, as seen in figures 13 and 14. The p.d.f. for the normalized number density of Lagrangian particles is depicted in figure 17(*d*). It had three and two peaks for diluted and non-diluted cases, respectively. For the diluted case, the first peak corresponded to particles inside the cell, which were the most and which are in the

dilute side (values lower than one). The second peak corresponded to the trajectories of the triple points and the third one to the locations between the collisions of the transverse waves and of the triple points. These two latter peaks are in the dense side (values greater than one). For the non-diluted case, only two peaks can be highlighted. The first peak corresponded to the particles inside the cell, as in the diluted case. The second peak corresponded more or less to a merge between the second and third peaks of the diluted case.

The results in §§ 4.1 and 4.2 highlighted that the dispersion of the Lagrangian particles was promoted behind the detonation front. The fact that the scaling for the variance of the $x-$displacement $\overline{x_i'^2}$ worked well using $(E_a/(RT_{vN}))x_{ind}$ suggested that the dispersion mainly came from a 1-D instability mechanism (figure 12*d*), mainly due to the pulsations of the leading shock.

The curvature of the leading shock front was responsible for the transverse dispersion of the particles (Mölder 2016), deviating the particles from horizontal detonation propagation direction (figures 13 and 14). Moreover, another source of transverse dispersion came from the presence of the reaction front. The value of $\overline{y_i'^2}/\overline{x_i'^2}$ was maximum around $2\tau_{ind}$ in the simulation results, which was indicative that the dispersion in the transverse direction increased around the reaction front (figure 12*b*). Indeed, Buckmaster & Ludford (1986) showed in a study on linear stability of steady, plane, overdriven detonation that the transverse velocity arose from the transverse derivative of the horizontal distance between the locations of the leading shock and the reaction front. Transverse waves clearly contributed to increase these effects (Emmons 1958).

In addition, jets induced fluctuations in the longitudinal dispersion (figures 10 and 11). The role of the jets on the fluctuations in the dispersion are expected to become more important for mixtures with lower isentropic coefficient at vN state (Lau-Chapdelaine, Xiao & Radulescu 2021; Sow *et al.* 2021; Taileb *et al.* 2021*b*).

4.3. *Relative dispersion*

The dispersion behind the front was further evaluated in terms of the relative dispersion in this subsection. The initial distance between two Lagrangian particles in the same pair was set to be the grid size upstream of the leading front, which is the minimum grid width. To distinguish the relative dispersion in the longitudinal and transverse directions, the following relative dispersions were evaluated:

$$r_{xy} = \left[(x_{p,i1} - x_{p,i2})^2 + (y_{p,i1} - y_{p,i2})^2\right]^{1/2}, \tag{4.6}$$

$$r_x = \left|x_{p,i1} - x_{p,i2}\right|, \tag{4.7}$$

$$r_y = \left|y_{p,i1} - y_{p,i2}\right|. \tag{4.8}$$

Here, $x_{p,i1}$ and $y_{p,i1}$ are x and y positions of the particle i1, and $x_{p,i2}$ and $y_{p,i2}$ are x and y position of the particle i2 which forms the pair with particle i1.

The 2-D Lagrangian instantaneous flow fields for the relative dispersion for both mixtures are shown in figures 18 and 19. The relative dispersion $\overline{r^2}_{xy}$ was the average value at the time from shock passage. The displayed value of r_{xy}^2 for each particle was the value averaged over its four pairs. Two main factors contributed to the highest values. First, the particles with higher relative dispersion experienced the shear layers emanating from the triple shock interaction and their curling to form the large-scale turbulent eddies. The second factor came from the presence of the boundary layer due to the velocity gradient.

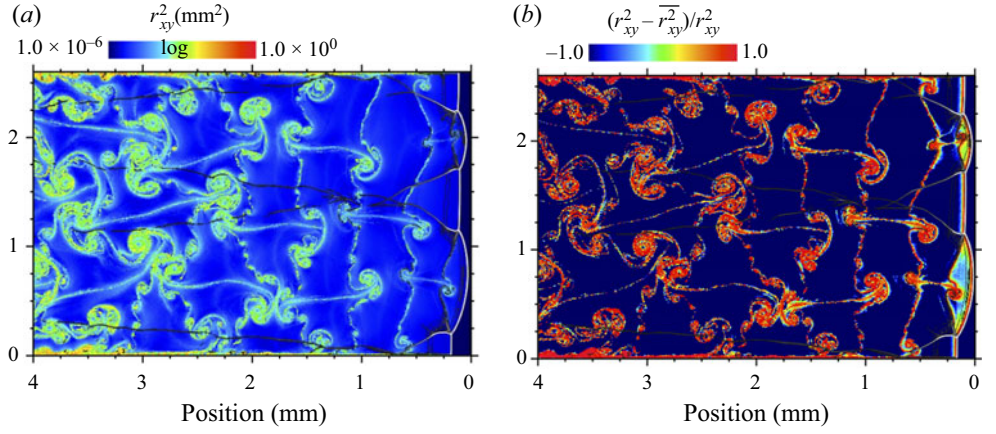

Figure 18. Diluted $2H_2$–O_2–7Ar mixture. The 2-D instantaneous Lagrangian flow fields, superimposed with Schlieren density. (*a*) Square of the relative dispersion r_{xy}^2; (*b*) normalized fluctuation of the square of the relative dispersion $(r_{xy}^2 - \overline{r^2}_{xy})/r_{xy}^2$.

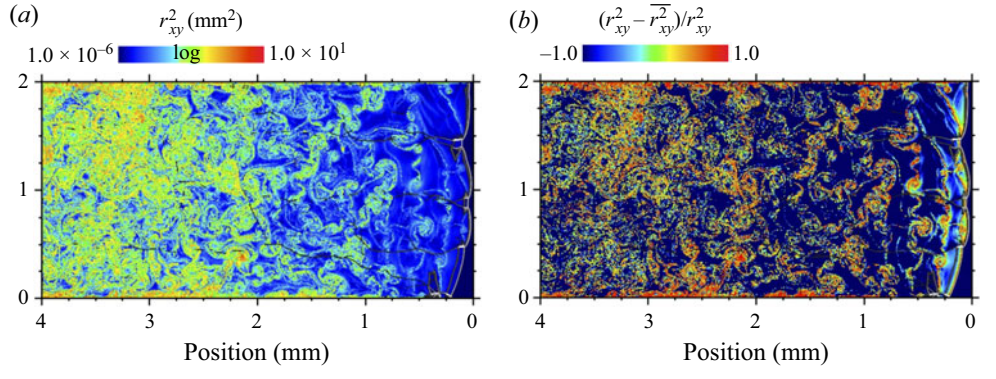

Figure 19. Non-diluted $2H_2$–O_2 mixture. The 2-D instantaneous Lagrangian flow fields, superimposed with Schlieren density. (*a*) Square of the relative dispersion r_{xy}^2; (*b*) normalized fluctuation of the square of the relative dispersion $(r_{xy}^2 - \overline{r^2}_{xy})/r_{xy}^2$.

The normalized deviation from the average $(r_{xy}^2 - \overline{r_{xy}{}^2})/r_{xy}^2$ highlighted these two main contributions (figures 18*b* and 19*b*). The relative dispersion was higher for the irregular mixture (figures 18*a* and 19*a*), with particles with higher relative dispersion being more dispersed inside the channel.

Figure 20 shows the square of average relative dispersion for $2H_2$–O_2–7Ar and $2H_2$–O_2 mixtures. The Lagrangian Favre average used for figure 20(*d*) based on the time from shock passage is described in § 4.4. In both mixtures, the average of r_x is higher than of r_y, highlighting again the anisotropy downstream of the leading front (figure 20*a*).

After some time, corresponding to some μs and far from the leading shock, a self-similar behaviour for both mixtures was found when the mean relative dispersion $\overline{r}_{xy}$ was scaled by the characteristic length scale χx_{ind}. The $(E_a/(RT_{vN}))x_{ind}$ length scale used in § 4.1 was not found to give nice results. Indeed, the relative dispersion of nearby particles is related to their difference of velocities that could be a result of the acceleration of reactive fronts,

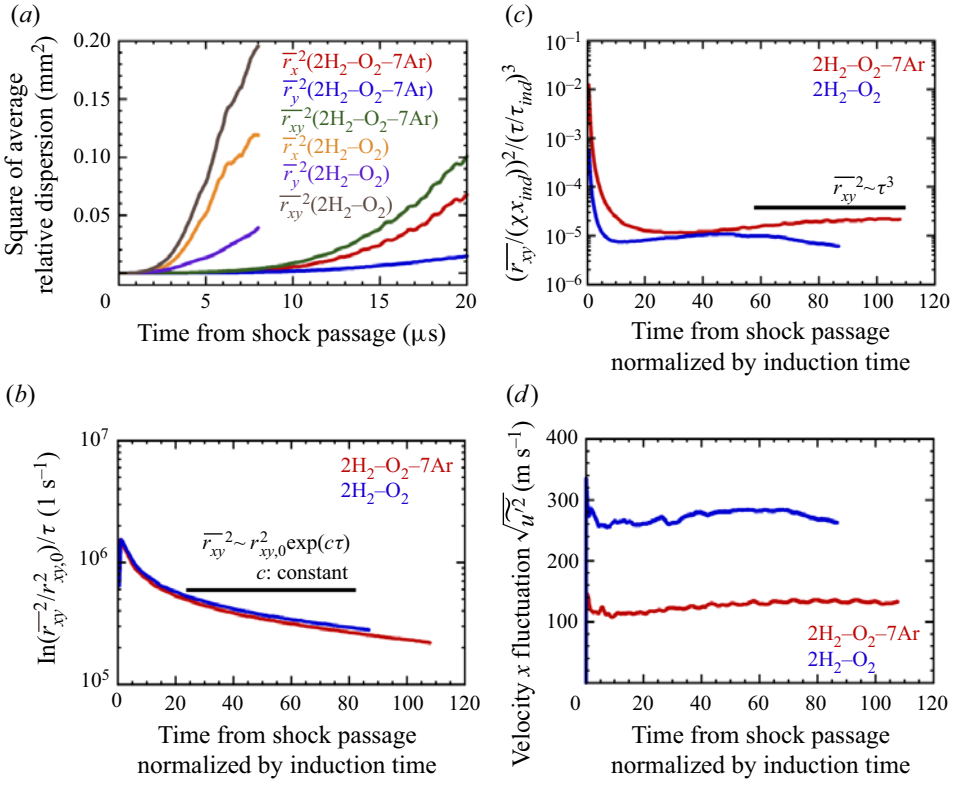

Figure 20. Time history of the average relative dispersion for 2H$_2$–O$_2$–7Ar and 2H$_2$–O$_2$ mixtures. (*a*) Square of average relative dispersion $\overline{r_x}^2$, $\overline{r_y}^2$, $\overline{r_{xy}}^2$, as a function of time passage τ; (*b*) logarithm of $\overline{r_{xy}}^2/\overline{r_{xy,0}}^2$ compensated by τ; (*c*) time history of normalized $(\overline{r_{xy}}/(\chi x_{ind}))^2$ compensated by normalized $(\tau/\tau_{ind})^3$; (*d*) x-velocity fluctuations $\sqrt{\widetilde{u'^2}}$. Here $\overline{r_{xy,0}}$ is the initial value for r_{xy}.

which is reflected by the non-dimensionalized acceleration parameter χ (Sharpe 2002; Radulescu, Sharpe & Bradley 2013; Tang & Radulescu 2013). Moreover, compensated by $(\tau/\tau_{ind})^3$, the non-dimensionalized pair dispersion from figure 20(*c*) agreed with the Richardson–Obukhov (R-O) law (Richardson 1926; Salazar & Collins 2009), meaning that $(r_{xy}/(\chi x_{ind}))^2$ scaled as $\sim (\tau/\tau_{ind})^3$. Darragh *et al.* (2021) in another context of high-speed premixed flames also found such scalings within some range but with different scalings. The exponential time dependence for inert flow (Babiano *et al.* 1990) did not hold (see figure 20*b*) for the lower times, the constant spanning over more than one order of magnitude. Indeed, the latter zone was the zone of the main heat release (see § 4.4 and Appendix C for further details on the estimation).

Figure 21 indicates the derivative of the relative dispersion with respect to time. The local exponent value is 3.77 ($50 < \tau/\tau_{ind} < 80$) and 3.38 ($20 < \tau/\tau_{ind} < 40$) for the diluted and non-diluted case, respectively. However, the non-dimensionalized time τ/τ_{ind} corresponding to the hydrodynamic thickness for both mixtures was around 50 (see Appendix C). Therefore, only the unstable case approached the R-O prediction within the detonation driving zone. The diluted case approached the R-O prediction only around the mean sonic surface. The initial distance in the stable case was larger than that in the unstable case, so the relaxation to the R-O scaling may also take longer (Bourgoin *et al.* 2006).

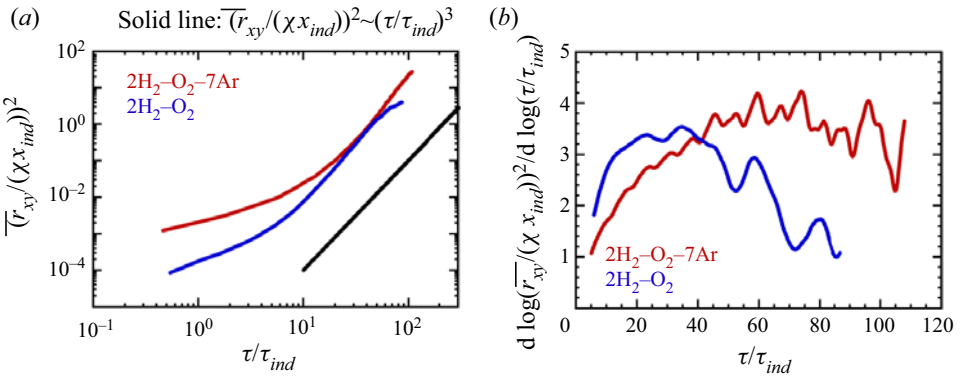

Figure 21. The $2H_2$–O_2–7Ar and $2H_2$–O_2 mixtures. (*a*) Time evolution of $(\overline{r_{xy}}/(\chi x_{ind}))^2$; (*b*) local scaling exponent of $\overline{r_{xy}}^2$ from $\mathrm{d}[\log(\overline{r_{xy}}/(\chi x_{ind}))^2]/\mathrm{d}[\log(\tau/\tau_{ind})]$.

The R-O law reads $r_{xy}^2/\tau^3 \sim \langle\epsilon\rangle$, with $\langle\epsilon\rangle$ being the turbulent energy dissipation rate (Salazar & Collins 2009). One can thus estimate $\langle\epsilon\rangle \sim \langle\delta u\rangle^2/\tau_{ind}$ as the ratio between the square of the x-velocity fluctuations δu and an induction time τ_{ind}. From figure 20(*d*), the ratio of the velocity fluctuations between the diluted and non-diluted cases after the induction and reaction zones is ∼2. Another estimation came from the turbulent energy dissipation rates $\langle\delta u\rangle_{non\text{-}diluted}/\langle\delta u\rangle_{diluted} \sim [\langle\epsilon\rangle_{non\text{-}diluted}/\langle\epsilon\rangle_{diluted} \times \tau_{ind,non\text{-}diluted}/\tau_{ind,diluted}]^{1/2} \sim 3$. This very good correspondence from such rough estimates seemed to indicate that after the main heat release zone, the more unstable the mixture was, the more turbulent the flow can be considered to be.

To evaluate the distribution in the relative dispersion, the p.d.f. for the relative dispersion r_{xy} is depicted in figure 22 for the diluted and non-diluted mixtures, respectively. The curves for the diffusive limit and the inertia regime were also included in figure 22(*c–f*) for comparison. These equations are recalled in Appendix C. The distribution becomes wider as the time from the shock passage increased (figure 22*a*,*b*). The same levels of relative dispersion were obtained much more rapidly in the non-diluted case. The relative dispersion is strongly non-Gaussian, with long tails developing, indicative of rare events. In figure 22(*c–f*), the relative dispersion has been rescaled by $\overline{r_{xy}}$ and a reasonably good collapse of the curves was obtained, showing that the process was self-similar in time, except for the rare events. A good fit for the tails of the p.d.f.s reads $A\exp(-\alpha(r_{xy}/\overline{r_{xy}})^\beta)$ (Jullien *et al.* 1999) and their coefficients are given in table 2. The exponent was approximately 0.35 and applied well for values of $r_{xy}/\overline{r_{xy}}$ between 5 and 15 for the diluted mixture, and was approximately 0.63 for values of $r_{xy}/\overline{r_{xy}}$ between 2 and 8 for the non-diluted one. The exponent for the unstable case agreed very well with Richardson's proposal of 2/3 (Richardson 1926) while that in the diluted case was below the latter value. The normalized relative dispersion for the non-diluted was less steep and higher for the most probable events in the intermediate range (see values of the fitted function in table 2), consistent with the fact that the mixture was considered to be more unstable near the leading shocks based on the reduced activation energy and χ parameters. What was more surprising was the presence of very rare events with high levels of relative dispersion for the diluted and regular case.

The probability of rare events was higher than that of Richardson's prediction (Buaria, Sawford & Yeung 2015) (see figure 22*e*,*f*). In the derivation of the p.d.f. by Richardson,

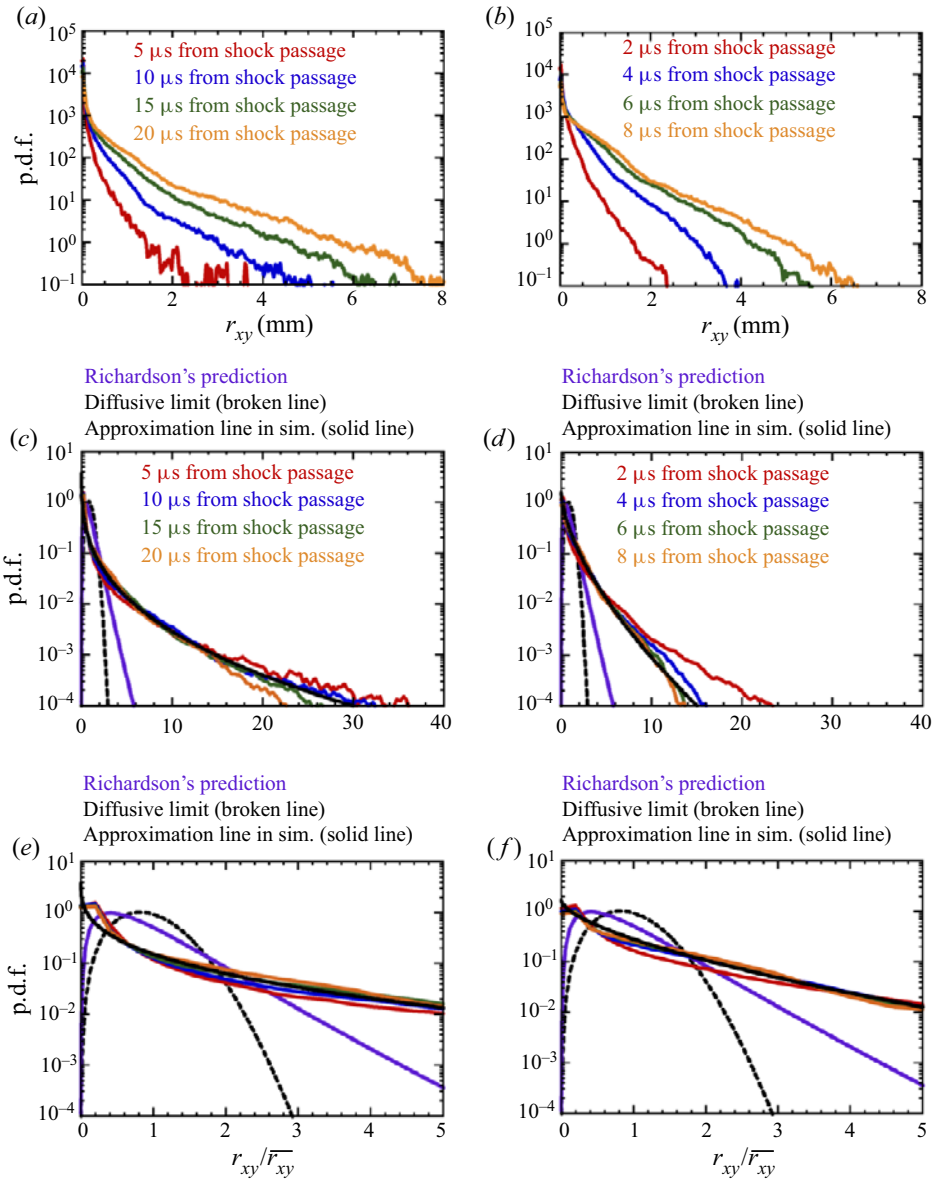

Figure 22. (*a*,*c*,*e*) The $2H_2$–O_2–7Ar mixture; (*b*,*d*,*f*) $2H_2$–O_2 mixture. (*a*,*b*) The p.d.f. for relative dispersion r_{xy}; (*c*,*d*) p.d.f. for $r_{xy}/\overline{r_{xy}}$; (*e*,*f*) enlarged view of p.d.f. for $r_{xy}/\overline{r_{xy}}$.

Mixture	A	α	β
$2H_2$–O_2–7Ar	3.78	3.21	0.35
$2H_2$–O_2	1.63	1.76	0.63

Table 2. Coefficients of the function approaching the p.d.f. of the normalized relative dispersion $r_{xy}/\overline{r_{xy}}$: p.d.f. $= A\exp(-\alpha(r_{xy}/\overline{r_{xy}})^{\beta})$ (Jullien, Paret & Tabeling 1999). The Richardson's prediction gives $\beta = 2/3$.

the dispersion process was described by a diffusive equation. This modelling was based on two assumptions (Boffetta & Sokolov 2002). The first one is that the dispersion process was self-similar in time. In our case, this assumption that the dispersion process was self-similar in time was valid (see figure 22*c–f*). The second one was that the velocity field was short correlated in time (Sokolov 1999). The relative velocity in quasi-Lagrangian coordinates (Boffetta *et al.* 1999) was then evaluated to check this validity of the latter assumption. The relative velocity in quasi-Lagrangian coordinates $\boldsymbol{v}^{QL}(\boldsymbol{R}, \tau)$ at time from shock passage τ was defined by the following equation:

$$\boldsymbol{v}^{QL}(\boldsymbol{R}, \tau) = \boldsymbol{v}(\boldsymbol{r_1}(\tau) + \boldsymbol{R}, \tau) - \boldsymbol{v}(\boldsymbol{r_1}(\tau), \tau). \tag{4.9}$$

Here, $\boldsymbol{v}(\boldsymbol{r}, \tau)$ is the Eulerian velocity field (u, v) at the position $\boldsymbol{r}$ and the time from the shock passage τ. The position of the Lagrangian particles at the time from the shock passage τ is $\boldsymbol{r_1}(\tau)$. The separation distance is $\boldsymbol{R}$. Note that only the particles that have passed the shock were taken into account. The velocities were obtained by interpolation of three nearby Eulerian cells (2.36).

The relative velocity in quasi-Lagrangian coordinates as a function of separation distance for $2H_2$–O_2–7Ar and $2H_2$–O_2 mixtures is shown in figure 23. When the separation distance was greater than the induction length, $(\boldsymbol{v}^{QL}(\boldsymbol{R}, \tau))^2$ was constant. However, when the separation distance was less than the induction length, regardless of the mixture regularity and time from shock passage, the square of relative velocity in quasi-Lagrangian coordinates was proportional to square of the separation distance, i.e. $(\boldsymbol{v}^{QL}(\boldsymbol{R}, \tau))^2 \propto (\boldsymbol{R}/x_{ind})^2$. This exponent of 2 was much higher than the exponent of 2/3, which is expected for the case of the Kolmogorov turbulence. Therefore, the velocity field behind the detonation front was not short time correlated. Thus, the dispersion process cannot be described by the diffusive equation proposed by Richardson. The probability of the rare event in the relative dispersion was then different from Richardson's prediction. In addition, the present finding that the velocity field behind the detonation front was different from that in the Kolmogorov turbulence can help us to develop a turbulent model for detonation. Indeed, Maxwell *et al.* (2017) conducted a numerical simulation with a compressible linear eddy model for large-eddy simulation for the highly unstable mixture of methane–oxygen. They had to increase the Kolmogorov constant from the theoretical prediction for incompressible 3-D Kolmogorov turbulence to match the experimental results. In addition, in 2-D simulations of the transition of a turbulent shock-flame complex to detonation, Maxwell, Pekalski & Radulescu (2018) decreased this constant. These changes of the constant may come from the fact that the velocity field behind the detonation was not that of a Kolmogorov turbulence.

The fact that the velocities were not short correlated below the induction length, and that the relative dispersion scaled with the χ parameter suggested that within the detonation driving zone, the heat release played a significant role. Indeed, $\chi = (x_{ind}/x_{reac})(E_a/(RT_{vN})) \propto (T/x_{reac})((\partial x_{ind}/\partial T)_{vN})$ is related to the rather rapid energy deposition, which promotes the dispersion of the particles on the reaction length scale.

The other possible reason for the departure of the probability of the rare event in the relative dispersion from Richardson's theory was the extreme events of the pair separating much faster and slower than the average. Scatamacchia, Biferale & Toschi (2012) reported in 3-D incompressible homogeneous and isotropic turbulence that the extreme events making much faster pair separation and much slower pair separation than the average induced the deviation from the behaviour in Richardson's theory. The relative dispersion behind the detonation front was much higher than the average for the Lagrangian particles, which experienced the shear layers emanating from the triple shock interaction and which

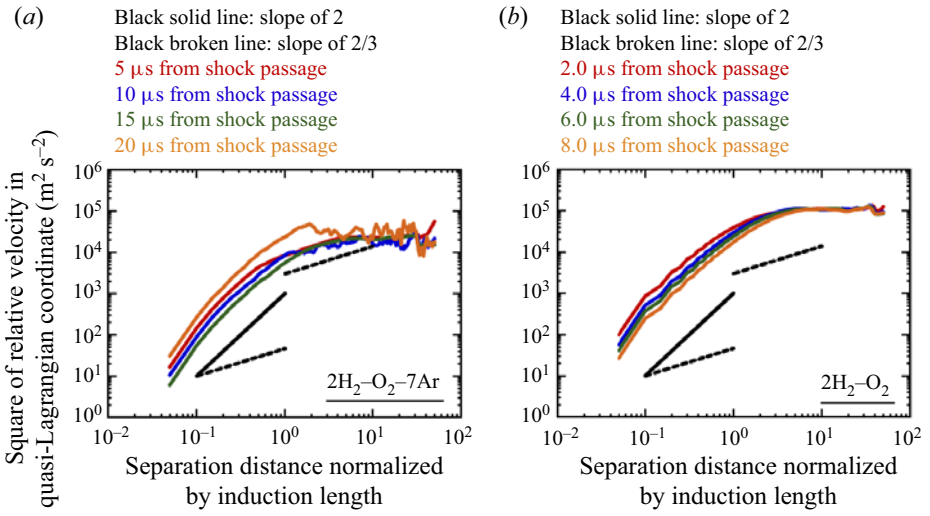

Figure 23. Square of relative velocity in quasi-Lagrangian coordinate as a function of separation distance normalized by induction length for various time from shock passage. (*a*) The $2H_2$–O_2–7Ar mixture; (*b*) $2H_2$–O_2 mixture. The black solid line is the curve with slope of 2 and the black broken line is the curve with slope of 2/3.

were located in the boundary layer. The other particles separated much slower (figures 18, 19). The possible effect of the presence of slip lines and boundary layers (figures 18, 19) on the higher possibility of the rare event was estimated by making a p.d.f. from the data with and without their presence. The criterion to distinguish the higher relative dispersion due to the slip lines and boundary layers was that the normalized fluctuation of the square of the relative dispersion $(r_{xy}^2 - \overline{r_{xy}}^2)/r_{xy}^2$ was higher than -0.95.

To evaluate the distribution in the relative dispersion for the data with and without the presence of the slip lines and boundary layers, a new p.d.f. for the normalized relative dispersion for the new set of data is depicted in figure 24. Regardless of the data based on the value of $(r_{xy}^2 - \overline{r_{xy}}^2)/r_{xy}^2$, the shapes of the p.d.f. were the same as in figure 22(*e*,*f*) and probability of the rare event in the relative dispersion remained higher than that from Richardson's theory. The same conclusion was obtained if the threshold was changed from -0.95 to 0.95 (not shown here). Thus, the presence of the slip lines and boundary layers was not the main factor for the probability of rare events in the relative dispersion to be higher than that from Richardson's prediction in the flow field behind the detonation front.

Another possible reason for this difference in the p.d.f. of the relative dispersion is that the turbulence has two cascades: an upward cascade coming from exothermic reactions and the downward Kolmogorov-like cascade (Radulescu 2003; Radulescu *et al.* 2005). In addition, the dispersion is slightly anisotropic in our 2-D case (see § 4.1), which can explain the deviations from results of isotropic turbulence (Xia *et al.* 2019). Moreover, the curves in the p.d.f. in the simulation are different from that in the diffusive regime.

4.4. *Eulerian and Lagrangian averaging procedures*

As a result of the dispersion, the same distance from the mean leading shock can be reached by several Lagrangian particles at different times, travelling different distances. Figures 25 and 26 depict the joint p.d.f. between the longitudinal distance from the shock x_s and (*a*) the time from shock passage τ and (*b*) the distance travelled by the particle $x_{xy,i}$.

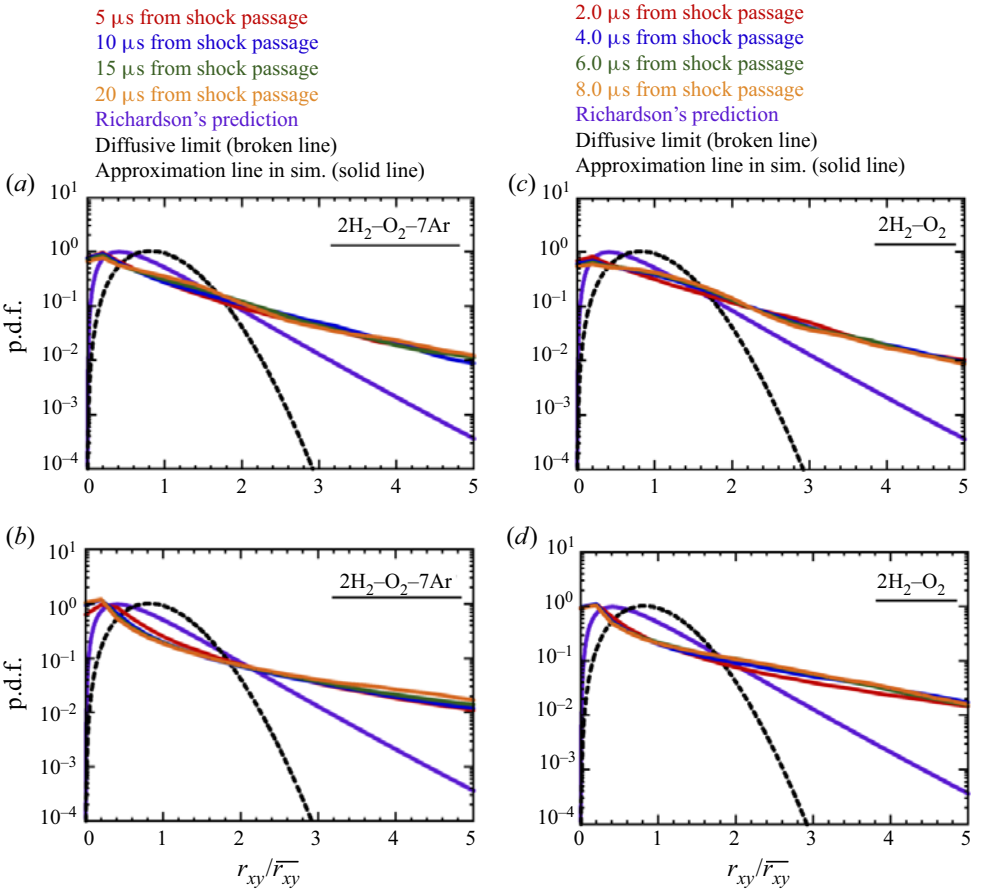

Figure 24. The p.d.f. for $r_{xy}/\overline{r_{xy}}$ from the categorized data (without slip lines and boundary layers) based on the value of $(r_{xy}^2 - \overline{r_{xy}}^2)/r_{xy}^2$: (*a*,*b*) $2H_2$–O_2–7Ar mixture; (*c*,*d*) $2H_2$–O_2 mixture. (*a*,*c*) The p.d.f. for $r_{xy}/\overline{r_{xy}}$ from the data whose $(r_{xy}^2 - \overline{r_{xy}}^2)/r_{xy}^2$ is higher than −0.95; (*b*,*d*) p.d.f. for $r_{xy}/\overline{r_{xy}}$ from the data whose $(r_{xy}^2 - \overline{r_{xy}}^2)/r_{xy}^2$ is lower than −0.95.

The width of the distribution for τ and $x_{xy,i}$ at fixed x_s increased as we moved away from the shock and as the mixture instability increased. A double peak can be observed in the regular case, whereas the dispersion became more uniform in the irregular case.

This subsection presents the comparison of the Favre average 1-D profiles in terms of Eulerian and Lagrangian points of view on the mean structure for the gaseous detonation. The Reynolds average values in the Eulerian mean procedure $\bar{G}_{\mathrm{EUL}}$ for the variable G are computed by (Watanabe *et al.* 2020)

$$\bar{G}_{\mathrm{EUL}}(x_s) = \frac{1}{H}\int_0^H \lim_{T_s\to\infty}\left(\frac{1}{T_s}\int_0^{T_s} G(x - x_{shock}(y,t), y, t)\,\mathrm{d}t\right)\mathrm{d}y. \tag{4.10}$$

Here, $x_{shock}(y,t)$ is the instantaneous x position of the leading shock front, which is not straight due to cellular instabilities, H is the channel width and T_s is the period of sampling, respectively. The longitudinal distance from the leading shock front $x_s = x - x_{shock}$ perpendicular to the propagation direction is used for the Eulerian averaging process. The time from the shock passage τ and the distance x_{xy} travelled by the Lagrangian particle

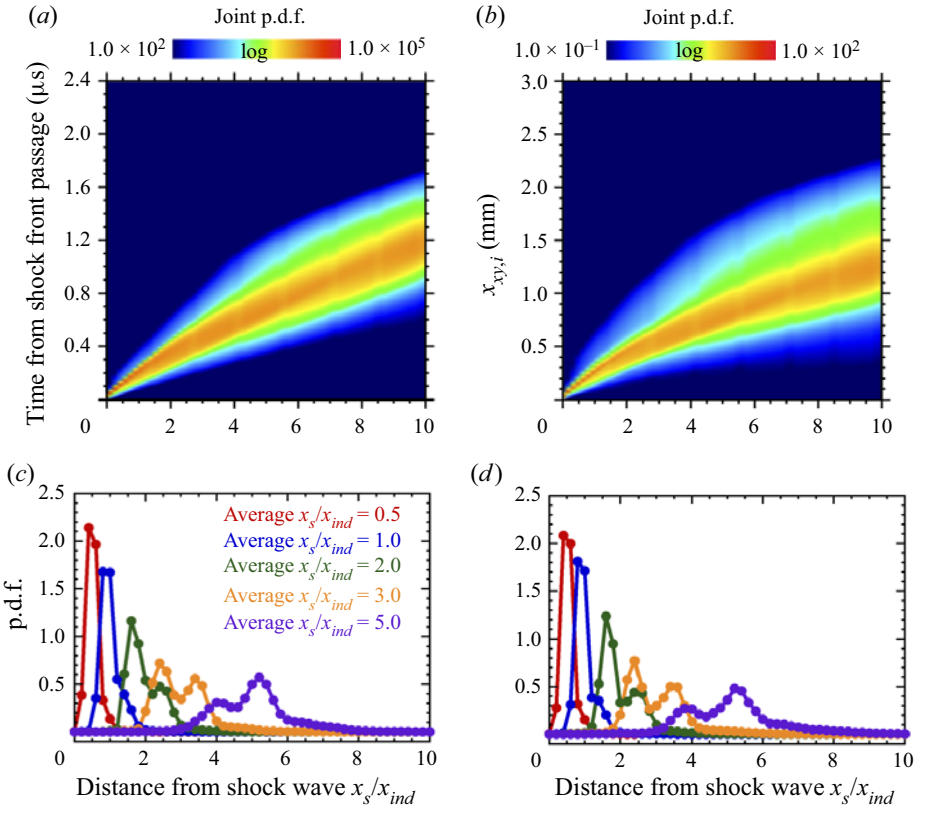

Figure 25. Distribution of τ and $x_{xy,i}$ as a function of the longitudinal distance from shock front in $2H_2$–O_2–7Ar mixture. (*a*) Joint p.d.f. between the longitudinal distance from shock front x_s and time from shock front passage τ, (*b*) joint p.d.f. between x_s and the distance travelled by the particle along the trajectory $x_{xy,i}$; (*c*) p.d.f. of x_s at several τ; (*d*) p.d.f. of x_s at several $x_{xy,i}$.

from shock passage can thus be also candidates for the Lagrangian averaging procedures. Two Lagrangian average procedures have been proposed. The first consisted in computing the Reynolds average values in the Lagrangian mean procedure based on the time from shock passage $\bar{G}_{\mathrm{LAG},time}$, as in (4.11); the second one consisted in computing the Reynolds average values in the Lagrangian average procedure based on the distance travelled by Lagrangian particle $\bar{G}_{\mathrm{LAG},dist}$, as in (4.12),

$$\bar{G}_{\mathrm{LAG},time}(\tau) = \frac{1}{N}\sum_{i=1}^{N} G_i(\tau), \tag{4.11}$$

$$\bar{G}_{\mathrm{LAG},dist}(x_{xy}) = \frac{1}{N}\sum_{i=1}^{N} G_i(x_{xy}), \tag{4.12}$$

where G_i is the value of the parameter at hand on particle i, $\tau = t - t_{shock}$ is the time elapsed from shock passage, x_{xy} is the postshock distance travelled by the particle and N is the number of particles sampled.

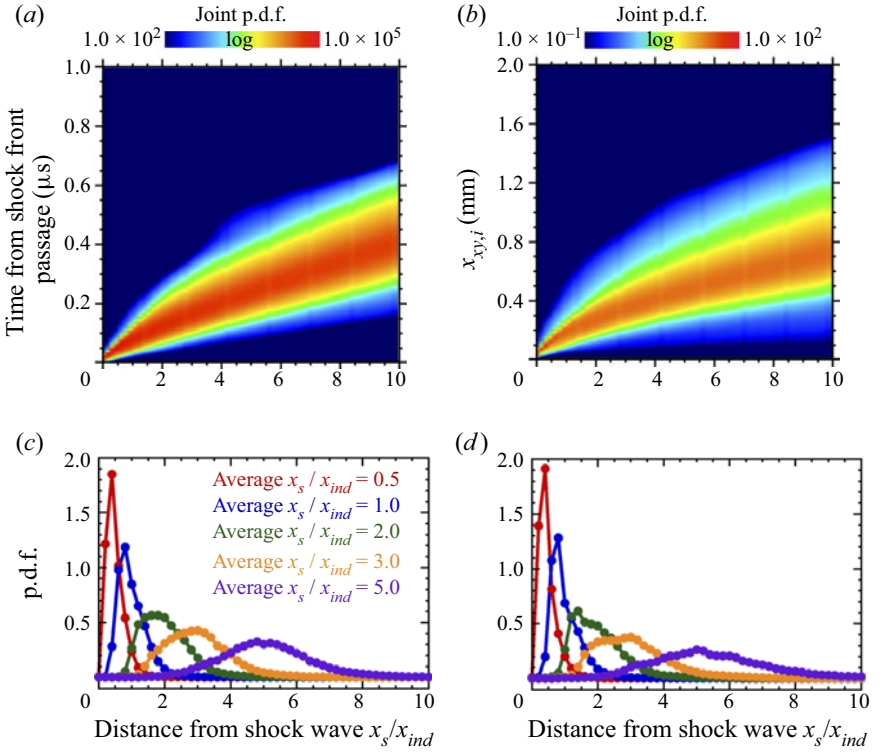

Figure 26. Distribution of τ and $x_{xy,i}$ as a function of the longitudinal distance from shock front in $2H_2$–O_2 mixture. (*a*) Joint p.d.f. between the longitudinal distance from shock front x_s and time from shock front passage τ. (*b*) Joint p.d.f. between x_s and the distance $x_{xy,i}$; (*c*) p.d.f. of x_s at several τ, (*d*) p.d.f. of x_s at several $x_{xy,i}$.

Then, from the different Reynolds averaging procedures, the Favre average quantities can be obtained from Reynolds averaged conservative variables $\tilde{\eta} = \overline{\rho\eta}/\bar{\rho}$, where η is the conservative variable (Favre 1965).

In order to enable the comparison between $\bar{G}_{\mathrm{EUL}}$ and $\bar{G}_{\mathrm{LAG},time}$, we need to map the time elapsed from shock passage up to the longitudinal distance from the shock location $x_{s,time}$. The following mapping will be used in (4.11):

$$x_{s,time} = \int_0^{\tau} (\bar{D} - \tilde{u})\, \mathrm{d}\tau. \tag{4.13}$$

Here, $\bar{D}$ is the average propagation velocity of the detonation front and is equal to D_{CJ} in the present simulation conditions. In order to map the distance travelled by the Lagrangian particle from the shock passage to the longitudinal distance from the shock location based on the distance travelled by the Lagrangian particle $x_{s,dist}$, the following mapping will be used in (4.12) for $\bar{G}_{\mathrm{LAG},dist}$:

$$x_{s,dist} = \int_0^{\tau} (\bar{D} - \tilde{u})\, \mathrm{d}t \quad \text{such as} \quad \mathrm{d}t = \mathrm{d}x_{xy} / \left[\tilde{u}^2 + \tilde{v}^2\right]^{1/2}. \tag{4.14}$$

Here, $\tilde{u}$ and $\tilde{v}$ are the Lagrangian Favre averages of the x and y components of the velocity in the laboratory frame. Figure 27 depicts the relations (4.13) and (4.14) between the distance from the shock front, the time from shock passage and the longitudinal distance

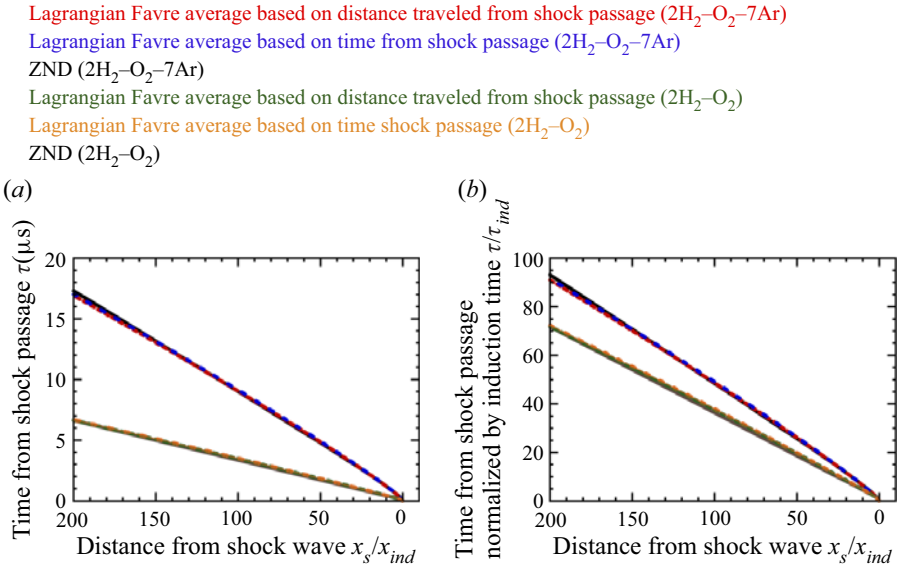

Figure 27. Lagrangian Favre average 1-D profiles for both mixtures (*a*) x_s / x_{ind} and τ, (*b*) x_s / x_{ind} and τ/ τ_{ind}.

from shock location. The results of the two Lagrangian procedures and the ZND model agreed well with each other, meaning that the procedures to convert the target values used in the Lagrangian procedures into the longitudinal distance from the shock front are appropriate.

The effects of the distance travelled by the particle and the time elapsed from the shock passage are not taken into account in the Eulerian procedure. However, the time elapsed from the shock passage is more relevant as far as chemical reactions are concerned. There are also differences between the two Lagrangian procedures. Indeed, the difference is more apparent especially in the boundary layer. Due to the lower velocity in the boundary layer, the distance x_{xy} does not increase as that in the core of the flow, for the same time elapsed from shock passage.

The comparison of the Favre average 1-D profiles in the instantaneous shock frame for $2H_2$–O_2–7Ar and $2H_2$–O_2 mixtures are depicted in figures 28 and 29, respectively. The frozen sound speed was used to estimate the Mach number in figures 28(*d*) and 29(*d*). The trends for the profiles of pressure, temperature and Mach number were nevertheless similar regardless of the Favre average procedure, either from the Eulerian or the Lagrangian point of view. Slight oscillations in Lagrangian Favre averages are observed near the front for the diluted case. In all cases, the profiles differed from that of the ZND solution. Indeed, Radulescu *et al.* (2007) and Sow *et al.* (2014) showed that the fluctuations delayed the energy deposition. Lalchandani (2022) developed a physical model that explained the slower rate of the heat release by the decaying of the shock velocity inside the cell.

As for the regular case (figure 28), the distributions of the chemical species, the thermicity and the other variables in Lagrangian and Eulerian results were almost identical. On the other hand, as for the irregular case, the width of the thermicity was wider (figures 28*c*,*e*,*f*,*g* and 29*c*,*e*,*f*,*g*). The increasing part of the curves was similar, whereas differences were apparent in the decreasing part of the thermicity, after its peak. All the other profiles then followed the same trend: Eulerian results matched the Lagrangian results before the peak of thermicity, with Lagrangian results decreasing more

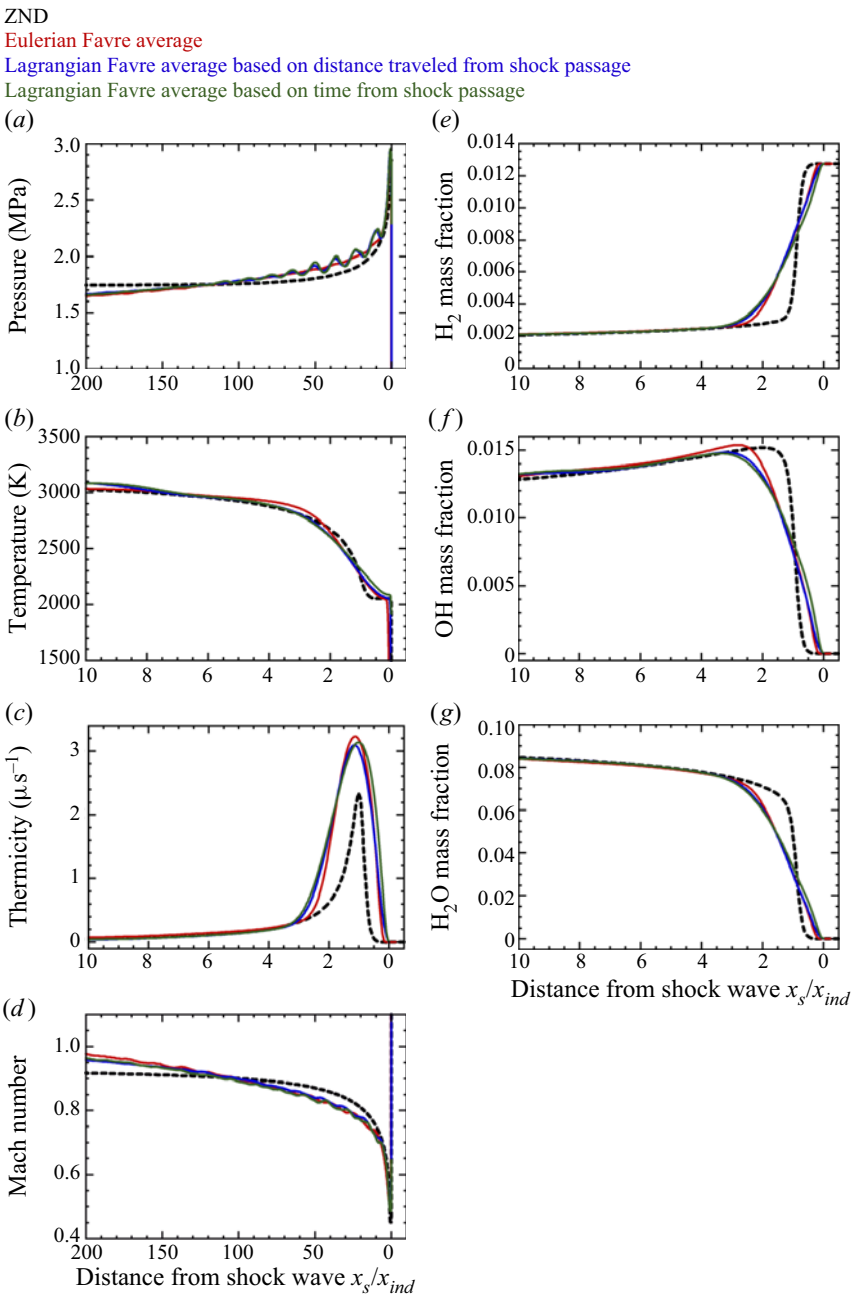

Figure 28. Favre average 1-D profiles in $2H_2$–O_2–7Ar mixture for (*a*) pressure, (*b*) temperature, (*c*) thermicity, (*d*) Mach number, (*e*) H_2 mass fraction, (*f*) OH mass fraction, and (*g*) H_2O mass fraction.

smoothly afterwards. Fewer differences were observed in the pressure and Mach number profiles. The maximum differences for the H_2 mass fraction were located after the peak of thermicity. They reached 12 % and 18 % between the Eulerian and Lagrangian time and distance averages for the diluted mixture and increased up to 33 % and 36 % for the other mixture.

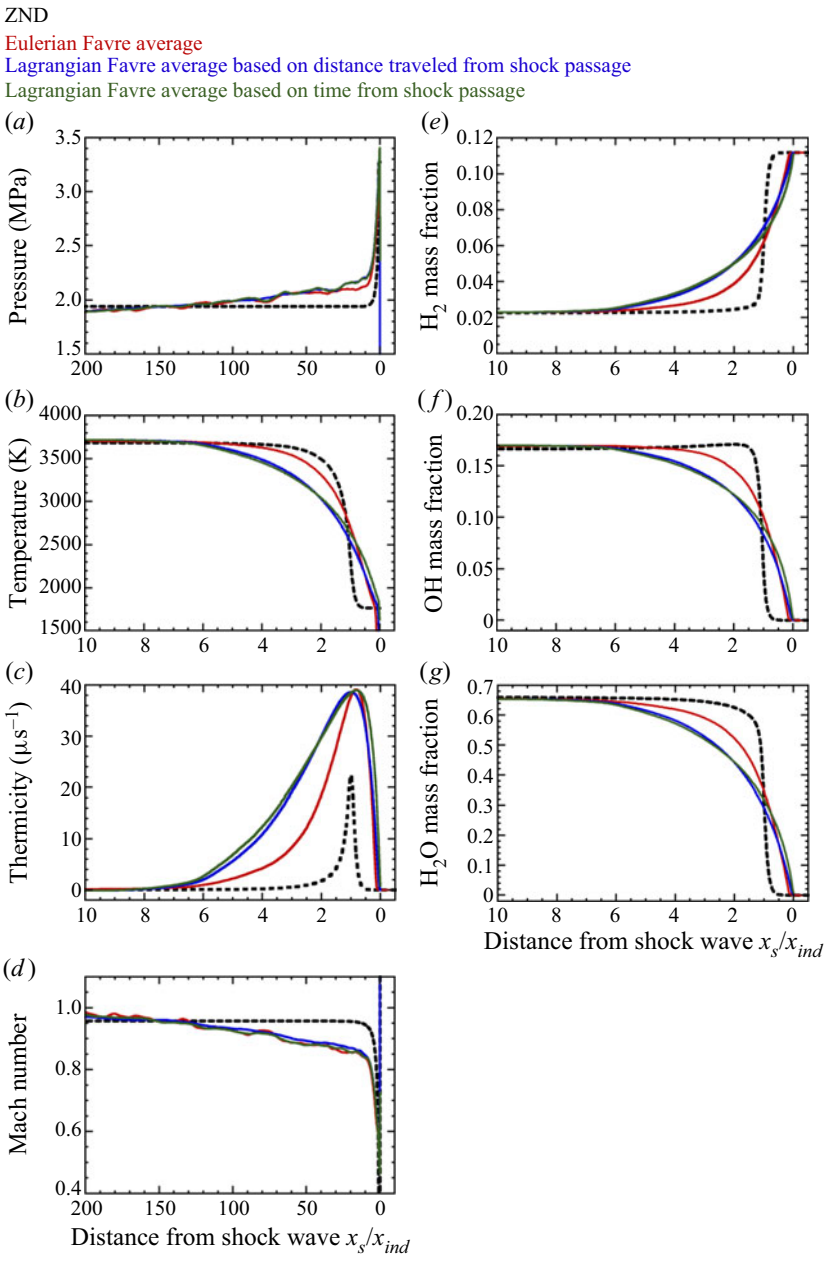

Figure 29. Favre average 1-D profiles in $2H_2$–O_2 mixture for (*a*) pressure, (*b*) temperature, (*c*) thermicity, (*d*) Mach number, (*e*) H_2 mass fraction, (*f*) OH mass fraction, and (*g*) H_2O mass fraction.

Based on the reduced activation energy and the related stability analysis for the emergence of longitudinal disturbances in 1-D cases, the mixtures could be classified as weakly and mildly unstable. Transverse disturbances then came into play in 2-D configurations. As argued at first by Radulescu *et al.* (2007) and by many others (Maxwell *et al.* 2017; Taileb *et al.* 2018; Reynaud *et al.* 2020; Sow *et al.* 2021), the fluctuations and the induced dispersion explain the differences between the mean quantities from

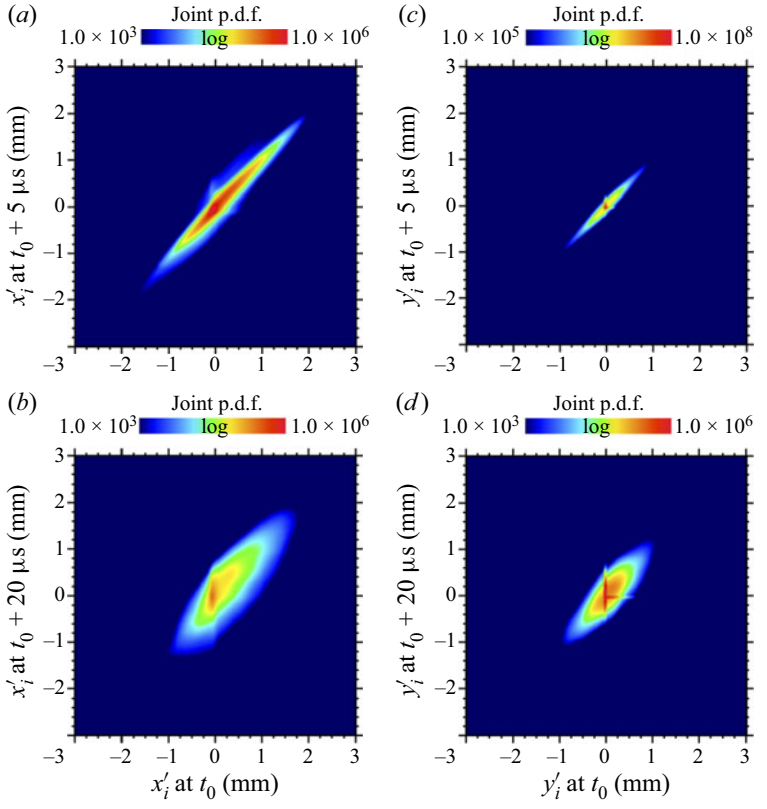

Figure 30. Joint p.d.f. between displacement fluctuations at t_0 and that at $t_0 + \tau_c$ in $2H_2$–O_2–7Ar mixture. (*a*) The x_i' displacement fluctuations with $\tau_c = 5\,\mu s$, (*b*) x_i' displacement fluctuations with $\tau_c = 20\,\mu s$, (*c*) y_i' displacement fluctuations with $\tau_c = 5\,\mu s$, (*d*) y_i' displacement fluctuations with $\tau_c = 20\,\mu s$.

numerical simulations and the ZND results. All dispersion quantities ($\overline{x_i'^2}$, $\overline{y_i'^2}$), when non-dimensionalized by $(E_a/(RT_{vN}))x_{ind}$ were found to be self-similar in the time τ/τ_{ind}. This good agreement suggests that the dispersion could result from a 1-D instability mechanism only. It may thus originate from the fluctuations of the leading shocks that induce the induction and reaction length fluctuations, with transverse waves being a necessary corollary.

On the other hand, the relative dispersion was also found to be self-similar in the time τ/τ_{ind}, after the main heat release zone, when the relative dispersion was normalized by χx_{ind}, with χ considered as a dimensionless acceleration. Both mixtures lie on either side on the neutral stability curve. Small values of χ imply that the pulses of heat release of neighbouring particles will overlap (Radulescu 2003). On the other hand, if this χ parameter is larger, gas-dynamic instabilities result from the lack of coherence of the power pulses and discreteness, and led to the deviations observed in the Eulerian and Lagrangian averaging processes after the peak thermicity for the irregular case.

The value of the specific heat ratio at vN state for the non-diluted case is 1.32 and was very close to the boundary where Mach bifurcation occurs due to jetting after triple point collision (Lau-Chapdelaine *et al.* 2021; Sow *et al.* 2021), which results in more mixing behind the front. For the range of γ_{vN} investigated in this study, the impact of compressibility (see figure 7 in Sow *et al.* (2021)) can be estimated to be low.

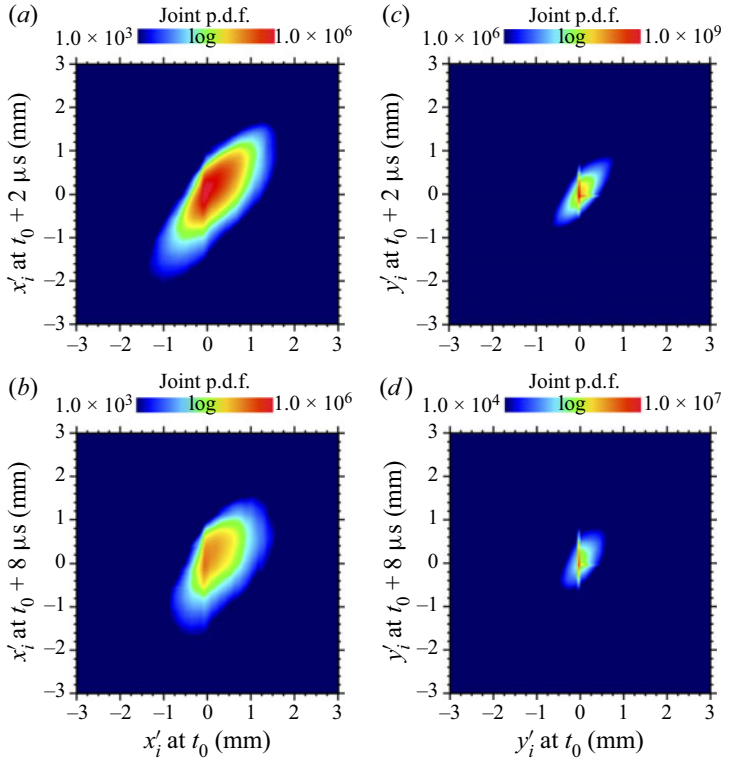

Figure 31. Joint p.d.f. between displacement fluctuations at t_0 and that at $t_0 + \tau_c$ in $2H_2$–O_2 mixture. (*a*) The x_i' displacement fluctuations with $\tau_c = 2\,\mu s$, (*b*) x_i' displacement fluctuations with $\tau_c = 8\,\mu s$, (*c*) y_i' displacement fluctuations with $\tau_c = 2\,\mu s$, (*d*) y_i' displacement fluctuations with $\tau_c = 8\,\mu s$.

Mixtures	τ_c (μs) - Figures	Correlation coefficients	
$2H_2$–O_2–7Ar	5 – figure 30(*a*)	$\sigma_{x_i'(t_0)x_i'(t_0+\tau_c)}$	0.98
	20 – figure 30(*b*)		0.89
	5 – figure 30(*c*)	$\sigma_{y_i'(t_0)y_i'(t_0+\tau_c)}$	0.98
	20 – figure 30(*d*)		0.90
$2H_2$–O_2	2 – figure 31(*a*)	$\sigma_{x_i'(t_0)x_i'(t_0+\tau_c)}$	0.84
	8 – figure 31(*b*)		0.70
	2 – figure 31(*c*)	$\sigma_{y_i'(t_0)y_i'(t_0+\tau_c)}$	0.88
	8 – figure 31(*d*)		0.81

Table 3. Correlation coefficients between displacements at t_0 and at $t_0 + \tau_c$.

Figures 30 and 31 show the joint p.d.f. of the fluctuations of the displacements $x_i' = (x_{p,i} - x_{p,i,0}) - \overline{(x_{p,i} - x_{p,i,0})}$ and $y_i' = (y_{p,i} - y_{p,i,0})$ at a certain instant t_0 with that at a later time $t_0 + \tau_c$, τ_c being equal to $\sim \tau_{HT}/2$ and $\sim 2\tau_{HT}$, where τ_{HT} is the time corresponding to the hydrodynamic thickness. If the motion were to be Brownian, the shape of the joint p.d.f. would correspond to a circle. Instead, in both cases, the joint p.d.f. lay along positive lines, meaning that they are positively correlated to each other. One can

Mixture	Characteristic lengths	Averaging procedure		
		Eulerian	Lagrangian (distance)	Lagrangian (time)
$2H_2$–O_2–7Ar	Induction length	1.1	1.1	1.0
	Reaction length	3.8	3.9	3.9
	Hydrodynamic thickness	115.0	117.7	117.0
	Average cell width	17.0	—	—
$2H_2$–O_2	Induction length	0.9	1.0	0.8
	Reaction length	0.8	0.8	0.8
	Hydrodynamic thickness	129.6	149.6	134.6
	Average cell width	14.4	—	—

Table 4. Characteristic lengths normalized by induction length for $2H_2$–O_2–7Ar and $2H_2$–O_2 mixtures. Non-dimensionalized cell widths are added for comparison. The Lagrangian (distance) stands for the averaging process, described by (4.12), (4.14) and Lagrangian (time) refers to procedure based on (4.11), (4.13).

see that the shape of the joint p.d.f. got rounder as time passed, all the more so as we got outside the mean detonation driving zone. Table 3 lists the correlation coefficients for the joint p.d.f. of figures 30 and 31 that were very high.

Table 4 lists the characteristic lengths for both mixtures for the different Favre averaging procedures. The induction and reaction lengths were almost the same. The position of the peak thermicity can be captured regardless of the average method. Only a slight variation was observed for the hydrodynamic thickness for the irregular case after the peak thermicity. Therefore, the Eulerian Favre average procedure gave the mean structure of the gaseous detonation with a reasonable accuracy.

5. Conclusions

Two-dimensional simulations with the Lagrangian particle tracking method were conducted for weakly and mildly unstable hydrogen-based mixtures at ambient conditions. Two new Lagrangian Favre average procedures, based on the distance travelled by the particle or the time from the shock passage were proposed and 1-D profiles were compared with those from the Eulerian procedure, based on the longitudinal distance from the shock front. The integral length was the hydrodynamic thickness that encompasses the mean detonation driving zone from the leading shock to the mean sonic line. The results from the Eulerian and Lagrangian averaging processes gave similar induction length, reaction length and hydrodynamic thickness. The Eulerian results gave the mean structure with a reasonable accuracy. As the mixture instability increased, the Lagrangian results were smoother after the thermicity peak than the Eulerian results.

Dispersion is inherent to the detonation driving zone, due to the fluctuations of the leading shock and its curvature, the presence of the reaction front, transverse waves, forward and backward jets, vortical structures and boundary layer. The latter was minor as the detonation was ideal with no losses. The main findings were that dispersion could be scaled with $(E_a/(RT_{vN}))x_{ind}$ and that the relative dispersion far from the shock, scaled by χx_{ind} with χ as a dimensionless acceleration. The fact that these instability parameters were successful for these scalings strongly suggests that the main mechanism driving the dispersion was the 1-D leading shock fluctuations, i.e. its decaying and amplification upon triple shock collision within the cell. For more highly unstable mixtures with larger $E_a/(RT_{vN})$ and χ, the presence of more frequent unburnt pockets of fresh gases along with

their burning mechanisms can circumscribe these findings. Moreover, the displacement fluctuations at a given time were positively correlated to the displacement fluctuations at a later time, corresponding to approximately the hydrodynamic thickness time scale.

The dispersion in the induction time scale was closely related to the cellular structure. Particles are not only accumulated between the locations of the transverse wave and triple point collisions but were also along the triple point trajectories. Another finding was that as the mixture instability increased, the contribution of the transverse waves along the triple point trajectories in the accumulation of the particles increased. The differences with the physical picture of cell size model relying on discrete blast dynamics were more apparent.

The induction process was completed within first half of the cell cycle in the diluted case, whereas more variation in the induction time could be found in the non-diluted case due to the higher activation energy and the presence of unburnt pockets. Within the induction time scale, the transverse dispersion was mainly due to the curvature of the leading shock. This effect was more pronounced near the edges of the cell and during the first part of the cell, when the leading detonation front was a Mach stem.

The detonation could be described as a two-scale phenomenon, especially for the unstable mixture. The first scale, of a few induction lengths approximately $5 \sim 10x_{ind}$, could be related to the main heat release zone, from the shock up to the vicinity of the peak thermicity. The influence of the transverse waves was still present. Indeed, the levels of y_i' were approximately those of x_i'. Then after a transient, a new zone was present. The transverse y_i' decreased, leading to small anisotropic dispersion ($[\overline{y_i'^2}/\overline{x_i'^2}]^{1/2} \sim 0.6$). The Richardson–Obukhov scaling law surprisingly still held, in the zone of small heat release after the peak thermicity, suggesting that classical non-reacting laws of turbulence may remain relevant. Only the unstable case approached the R-O scaling within the mean detonation driving zone.

The dispersion of the Lagrangian particles was promoted behind the detonation front. We could try to sort out the production of these fluctuations: x displacements due to the decaying detonation front (1-D instability mechanism), then y displacements due to the curvature of the leading inert shock front and the presence of the reaction front (due to density ratio). The variation of the distance between the leading shock and the reaction front in the transverse direction induced further transverse dispersion (maximum of $\overline{y_i'^2}/\overline{x_i'^2}$ around $2\tau_{ind}$). Even if the reactive transverse waves were present in the diluted case, and some unburnt pockets in the non-diluted case, these differences do not manifest themselves on the dispersion of the Lagrangian particles (collapse of the histories of scaled $\overline{x_i'^2}/(E_a/(RT_{vN}x_{ind}))^2$ and $\overline{y_i'^2}/\overline{x_i'^2}$). In our case, due to high isentropic coefficients, the jets have not induced any cell bifurcation.

The study of the derivative of the relative dispersion with respect with time showed that after the main heat release, the relative dispersion relaxed towards the Richardson–Obukhov regime (exponent near 3), especially for the non-diluted case. The influence of the vortical motions coming from the jets and the slip lines, the fading of the transverse waves cannot be ignored in this transition.

Moreover, the exponent of the p.d.f. for the relative dispersion was also consistent with Richardson's prediction in the unstable case. Furthermore, the p.d.f. for the relative dispersion was self-similar in time. Nevertheless, the velocity field was not short time correlated with a separation distance below the induction length, meaning that the dispersion process could not be described by the diffusive equation. The relative dispersion scaled with the χ parameter, which suggested that the rapid energy deposition on the reaction length scale also contributed to this phenomenon.

In addition, the present finding on the velocity field behind the detonation front can help to develop a turbulent model for detonation. Lagrangian averaging can have a merit over that from Eulerian results despite its higher computational cost. Conditional p.d.f. as in dispersed detonation flows (Watanabe *et al.* 2021) could improve our understanding of the links between pressure, vortical, entropy modes and chemistry in detonation.

Acknowledgements. A.C. and H.W. would like to thank V. Robin from Institut Prime for many fruitful discussions and advice. H.W. and A.C. are very grateful for the comments and suggestions by the anonymous referees during the revision of the manuscript.

Funding. This research was subsided by JSPS KAKENHI grant number JP20K22391 (Grant-in-Aid for Research Activity Start-up), JP21K14094 (Grant-in-Aid for Early Career Scientists), JP19J12758 (Grant-in-Aid for Specially Promoted Research), the Paloma Environmental Technology Development Foundation, and the CPER FEDER Project of Région Nouvelle Aquitaine and pertains to the French government program 'Investissements d'Avenir' (EUR INTREE, reference ANR-18-EURE-0010). H.W. is supported by JSPS Overseas Research Fellowships.

Declaration of interests. The authors report no conflict of interest.

Author ORCIDs.
Hiroaki Watanabe https://orcid.org/0000-0003-1646-9391;
Akiko Matsuo https://orcid.org/0000-0003-0526-5502;
Ashwin Chinnayya https://orcid.org/0000-0002-8728-2148;
Noboru Itouyama https://orcid.org/0000-0002-7508-4611;
Akira Kawasaki https://orcid.org/0000-0003-4532-3682;
Ken Matsuoka https://orcid.org/0000-0002-8730-9937;
Jiro Kasahara https://orcid.org/0000-0002-6524-1345.

Appendix A. Assessment of numerical convergence

In this appendix, the numerical convergence was assessed to check the effect of the grid resolution on the simulation results. The high computational cost for the numerical simulations with the Lagrangian particle tracking method prevented us using higher grid resolution than that used in the present study. According to previous studies, the present grid resolution satisfied the requirement for the grid resolution for the convergence of the 1-D average profiles (Reynaud *et al.* 2017, 2020) for both mixtures and a reasonable physical structure in the instantaneous 2-D flow field (Mazaheri *et al.* 2012) in $2H_2$–O_2–7Ar mixture.

The numerical convergence was assessed by comparing the simulation results using a coarser grid, which was two times larger than the one used for the main results. The same simulation conditions were used and the propagation velocity was the same regardless of the grid resolution. In addition, the average cell width in the simulation from the manual measurement of 150 and 300 cells for the $2H_2$–O_2–7Ar and $2H_2$–O_2 mixtures in the coarse grid was 1.3 and 0.7 mm, respectively. The average cell width agreed well between the two different grid resolutions.

The comparison of the average dispersion between the two different grid resolutions was shown in figure 32. Although minor differences were observed, the profiles for average dispersion with different grid resolutions were similar (figure 32).

The effect of the grid resolution on the relative dispersion was also evaluated. The initial distance between two particles in the same pair was doubled, as compared with the computations shown in § 4.3. Figure 33 depicts the average relative dispersion for $2H_2$–O_2–7Ar and $2H_2$–O_2 mixtures. The profiles were similar between the two grid resolutions. In the $2H_2$–O_2 mixture, the differences could be seen, as the time from shock

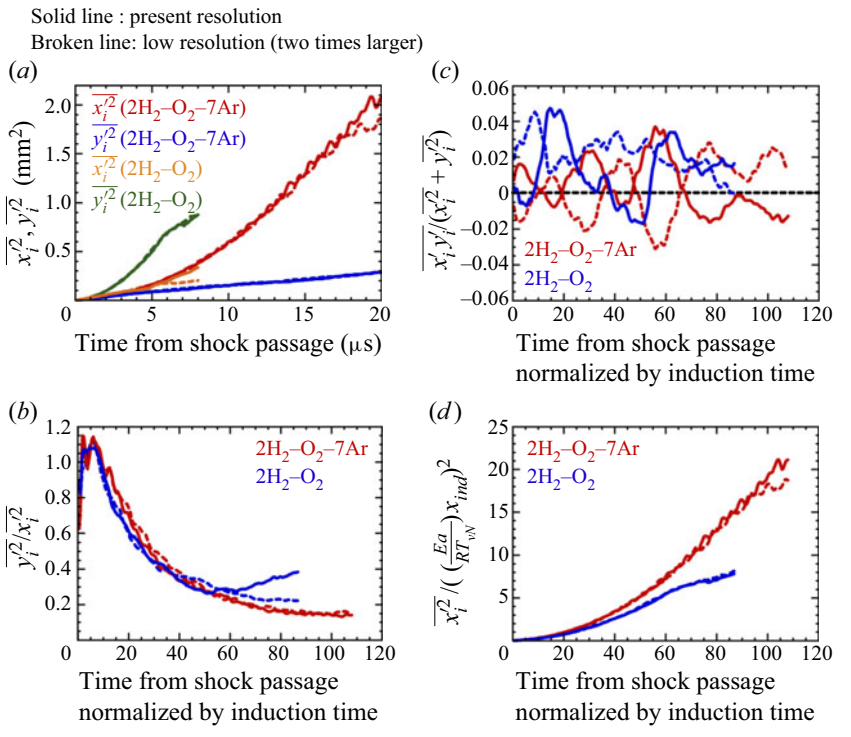

Figure 32. Average dispersion in $2H_2$–O_2–7Ar and $2H_2$–O_2 mixtures with two different grid resolutions. (*a*) Time history of $\overline{x_i'^2}$ and $\overline{y_i'^2}$, (*b*) $\overline{y_i'^2}/\overline{x_i'^2}$ as a function of τ/τ_{ind}, (*c*) $\overline{x_i'y_i'}/(\overline{x_i'^2}+\overline{y_i'^2})$, (*d*) $\overline{x_i'^2}/(E_a/(RT_{vN})x_{ind})^2$ as a function of τ/τ_{ind}.

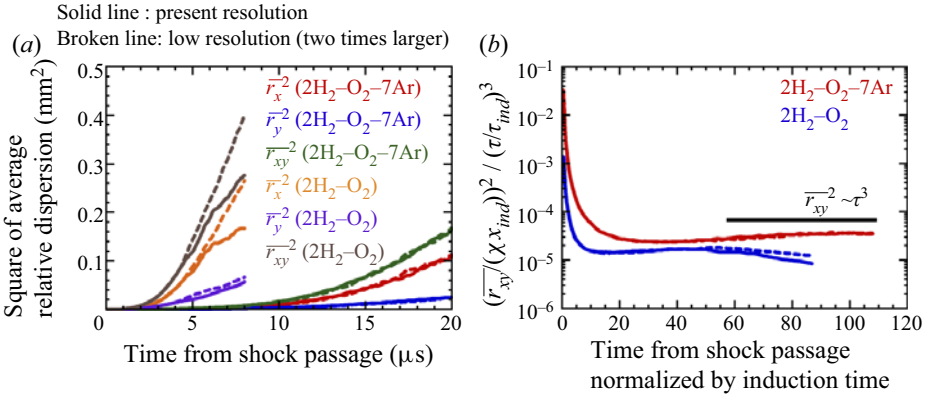

Figure 33. Average relative dispersion in $2H_2$–O_2–7Ar and $2H_2$–O_2 mixtures with two different grid resolutions. (*a*) Average relative dispersion $\overline{r_x}^2$, $\overline{r_y}^2$, $\overline{r_{xy}}^2$, as a function of time passage τ, (*b*) time history of normalized $(\overline{r_{xy}}/(\chi x_{ind}))^2$ compensated by normalized $(\tau/\tau_{ind})^3$.

passage increased. Nevertheless, the average relative dispersion $\bar{r}_{xy}$ normalized by the characteristic length scale χx_{ind} as a function of the time from shock front passage τ/τ_{ind} showed similar trends for both grid resolutions, meaning that the scaling worked well and that the R-O law still held.

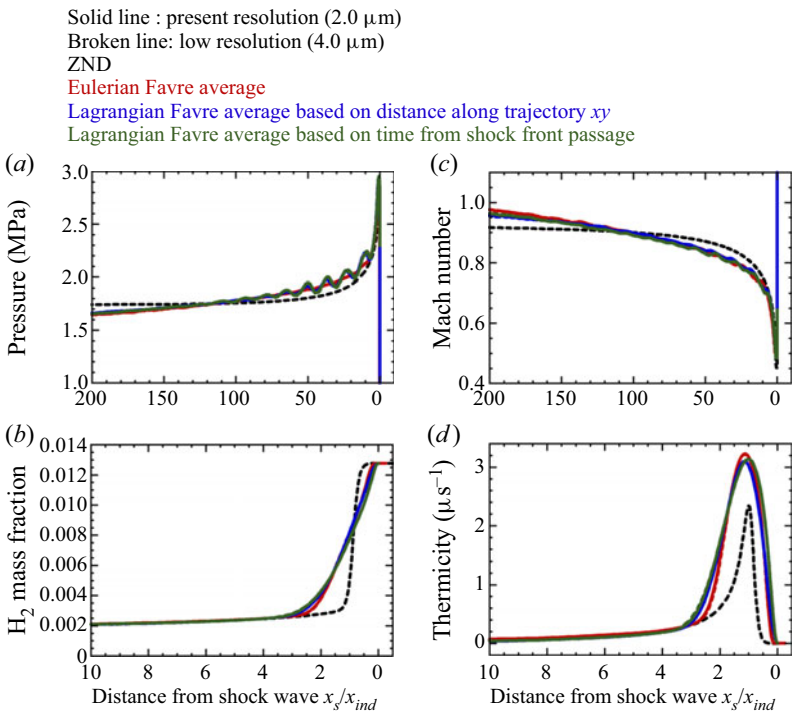

Figure 34. Favre average 1-D profiles in $2H_2$–O_2–7Ar mixture with two different grid resolutions for (*a*) pressure, (*b*) H_2 mass fraction, (*c*) Mach number, (*d*) thermicity.

The comparisons of the Favre average 1-D profiles in the instantaneous shock frame from Eulerian and Lagrangian points of view using the two different grid resolutions for $2H_2$–O_2–7Ar and $2H_2$–O_2 mixtures are depicted in figures 34 and 35. The characteristic lengths estimated from the Favre average 1-D profiles in the coarse grid are listed in table 5.

In the $2H_2$–O_2–7Ar mixture, the Favre average 1-D profiles for pressure, H_2 mass fraction, Mach number and thermicity were well converged between the two different grid resolution regardless of the Favre average procedure (figure 34). The Favre average 1-D profiles from Eulerian procedure for the $2H_2$–O_2 mixture were also similar between the two different grid resolutions (figure 35), except some minor differences.

Therefore, the characteristic lengths were similar between the two different grid resolutions. Moreover, the mean structure was also well captured by the present grid resolution (tables 4 and 5). This observation on the effect of grid resolution on the mean structure was in line with the previous studies (Reynaud *et al.* 2017, 2020).

Thus, the profiles used for the analysis were well captured in the present grid resolution, and the conclusions on the Lagrangian dispersion and the mean structure in this study were not called into question by the numerical resolution.

Appendix B. Evaluation of anisotropy from the fluctuations in displacement

The dispersion was anisotropic (see figure 12*b*), where $[\overline{y_i'^2}/\overline{x_i'^2}]^{1/2}$ decreased from 1 near the front to 2/3 at the end of the detonation driving zone. To quantify further this dispersion, the joint p.d.f. between x_i' and y_i' is depicted in figures 36 and 37 for different instants to show their evolution. The centres are determined where $x_i' = y_i' = 0$.

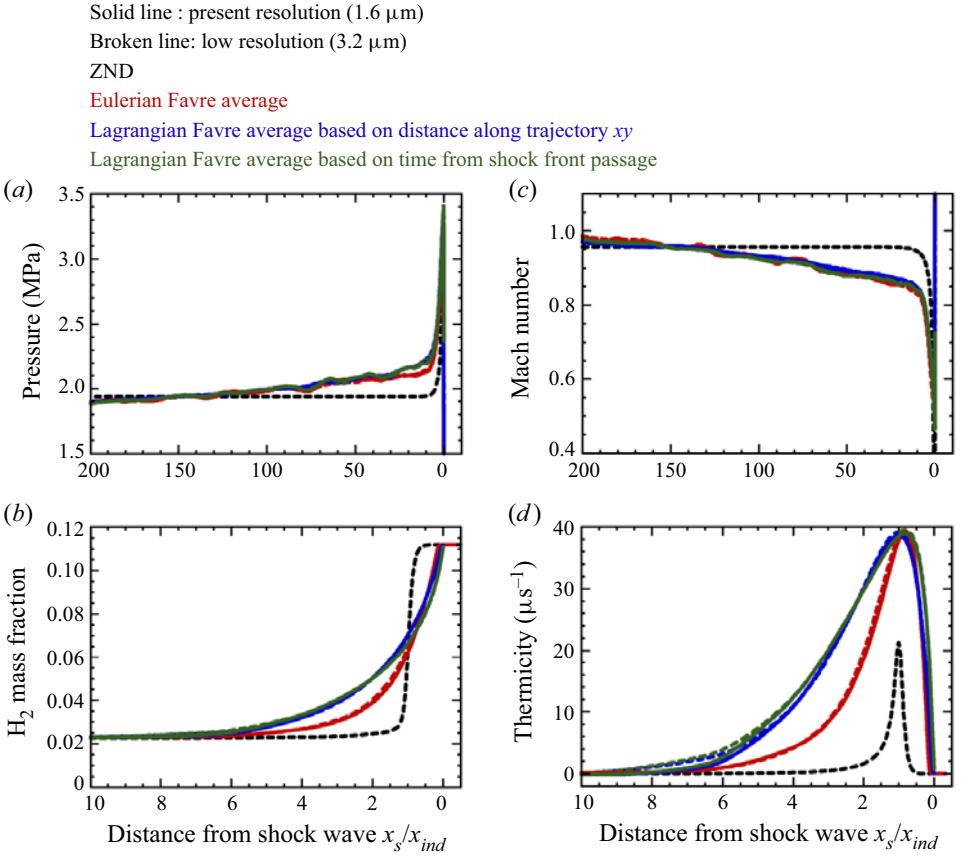

Figure 35. Favre average 1-D profiles in $2H_2$–O_2 mixture with two different grid resolutions for (*a*) pressure, (*b*) H_2 mass fraction, (*c*) Mach number, (*d*) thermicity.

Mixture	Characteristic lengths	Averaging procedure		
		Eulerian	Lagrangian (distance)	Lagrangian (time)
$2H_2$–O_2–7Ar	Induction length	1.1	1.1	1.0
	Reaction length	3.8	3.9	3.9
	Hydrodynamic thickness	114.4	117.9	116.2
	Average cell width	17.0	—	—
$2H_2$–O_2	Induction length	0.9	1.0	0.8
	Reaction length	0.8	0.8	0.8
	Hydrodynamic thickness	129.2	154.8	154.4
	Average cell width	14.2	—	—

Table 5. Characteristic lengths normalized by induction length for $2H_2$–O_2–7Ar and $2H_2$–O_2 mixtures in the coarse grid resolution. Non-dimensionalized cell widths are added for comparison. The Lagrangian (distance) stands for the averaging process, described by (4.12), (4.14) and Lagrangian (time) refers to procedure based on (4.11), (4.13).

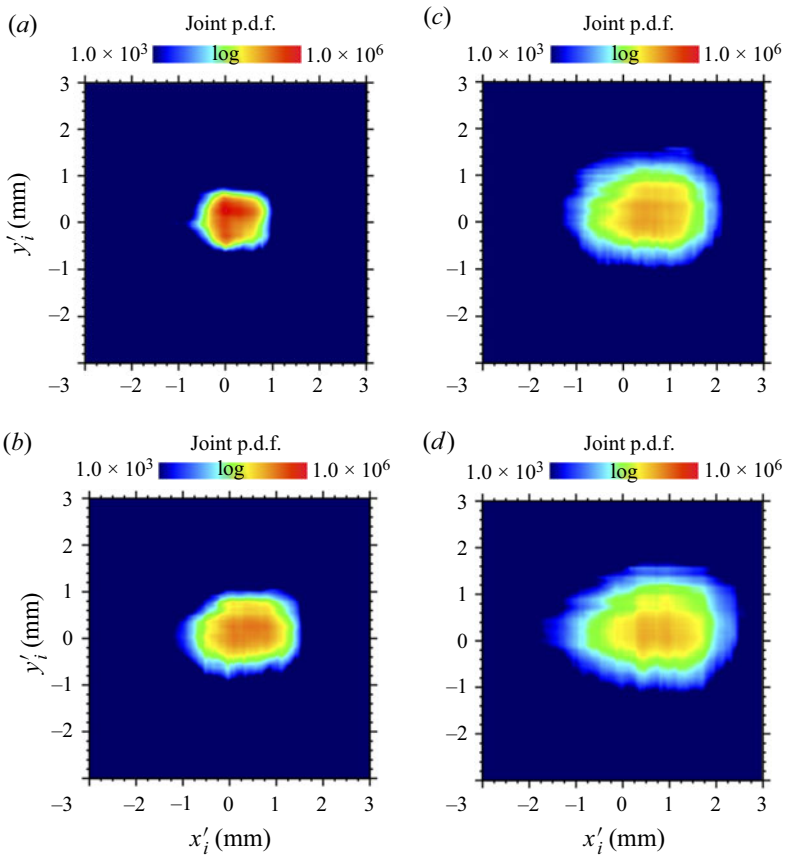

Figure 36. Joint p.d.f. for $2H_2$–O_2–7Ar between the fluctuations of longitudinal displacements x_i' and that of the transverse displacements y_i' for different times from shock passage: (*a*) 5 µs; (*b*) 10 µs; (*c*) 15 µs; (*d*) 20 µs.

The boundary of the joint p.d.f. shape was taken at 10^4. The roundness and relative roundness were then evaluated as a measurement of the anisotropy:

$$R_n = \max((e_{x,p} + e_{x,n}), (e_{y,p} + e_{y,n})) - \min((e_{x,p} + e_{x,n}), (e_{y,p} + e_{y,n})), \tag{B1}$$

$$R_{n,r} = R_n / \max((e_{x,p} + e_{x,n}), (e_{y,p} + e_{y,n})). \tag{B2}$$

Here, $e_{x,p}$ and $e_{x,n}$ are the distances from the centre to the edges of the boundary in the x-axis, and in the same way for $e_{y,p}$ and $e_{y,m}$ in the y-axis. The roundness and relative roundness denote the degree of the symmetry of the joint p.d.f. and its relative magnitude, respectively. Their values are listed in table 6. The roundness was not zero and increased as time passed for both mixtures, which means that dispersion became anisotropic. However, the relative roundness rapidly saturated to 35 % and to 40 % for both mixtures, values of which are consistent with the ratio of $1 - [\overline{y_i'^2}/\overline{x_i'^2}]^{1/2} \sim 1/3$ found previously.

Appendix C. The p.d.f. of the relative dispersion, correlation coefficients and characteristic time scales

The curves for the diffusive limit and the inertia regime are recalled here as they were included in figure 22(*c–f*) for comparison. The p.d.f. for the relative dispersion in the

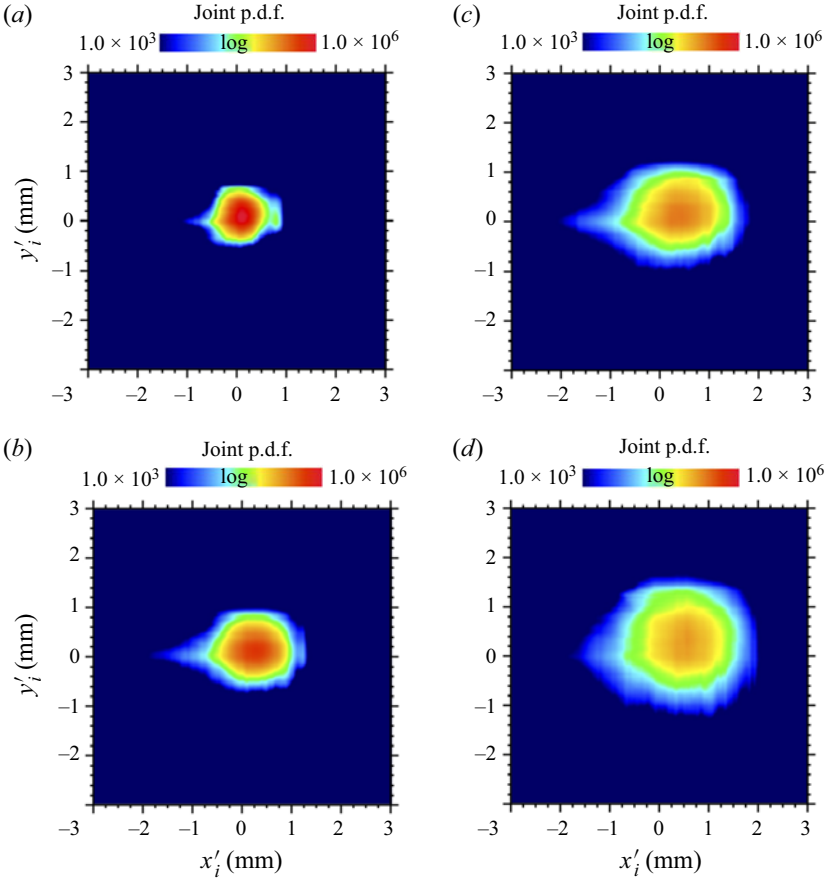

Figure 37. Joint p.d.f. for $2H_2$–O_2 between the fluctuations of longitudinal displacements x_i' and that of the transverse displacements y_i' for different times from shock passage: (*a*) 2 µs; (*b*) 4 µs; (*c*) 6 µs; (*d*) 8 µs.

Mixture	Value				
	Time from shock passage (µs)	5.0	10.0	15.0	20.0
	Roundness (mm)	0.51	0.55	0.97	0.89
$2H_2$–O_2–7Ar	Relative roundness (%)	36.0	28.0	35.0	30.0
	Offset in *x* direction (mm)	0.14	0.31	0.49	0.61
	Offset in *y* direction (mm)	0.07	0.13	0.28	0.30
	Time from shock passage (µs)	2.0	4.0	6.0	8.0
	Roundness [mm]	0.55	0.86	0.77	1.38
$2H_2$–O_2	Relative roundness (%)	39.0	45.0	34.0	46.0
	Offset in *x* direction (mm)	0.11	0.11	0.23	0.38
	Offset in *y* direction (mm)	0.12	0.14	0.22	0.29

Table 6. Roundness and offset from the centre in joint p.d.f. for the fluctuations of longitudinal displacements and that of the transverse displacements.

Mixture	Characteristic times	Averaging procedure		
		Eulerian	Lagrangian (distance)	Lagrangian (time)
$2H_2$–O_2–7Ar	Induction time	0.9	1.0	0.9
	Reaction time	1.7	1.7	1.7
	Hydrodynamic thickness time	55.5	56.3	56.4
	Characteristic time for cell (cell length/D_{CJ})	6.6	—	—
$2H_2$–O_2	Induction time	0.6	0.7	0.6
	Reaction time	0.3	0.3	0.3
	Hydrodynamic thickness time	48.4	54.7	50.0
	Characteristic time for cell (cell length/D_{CJ})	4.3	—	—

Table 7. Characteristic times normalized by induction time for $2H_2$–O_2–7Ar and $2H_2$–O_2 mixtures. The Lagrangian (distance) stands for the averaging process, described by (4.12), (4.14) and Lagrangian (time) refers to procedure based on (4.11), (4.13).

diffusive limit f_{diff} is given by (Buaria *et al.* 2015)

$$\text{p.d.f.}_{diff} = 3\sqrt{6/\pi}(r_{xy}/\overline{r_{xy}})^2 \exp\left[-\tfrac{3}{2}(r_{xy}/\overline{r_{xy}})^2\right]. \tag{C1}$$

Richardson predicted the p.d.f. for the relative dispersion in the inertia regime p.d.f.$_{inertia}$ as follows (Sawford, Pope & Yeung 2013):

$$\text{p.d.f.}_{inertia} = \left(\frac{1144}{81}\right)^{3/2}\left(\frac{2187}{560\sqrt{\pi}}\right)(r_{xy}/\overline{r_{xy}})^2 \exp\left[-\frac{9}{4}\left(\frac{1144}{81}\right)^{1/3}(r_{xy}/\overline{r_{xy}})^{2/3}\right]. \tag{C2}$$

The characteristic times normalized by the induction time for both mixtures for the different Favre averaging procedure are listed in table 7.

The correlation coefficients between the displacements at t_0 and at $t_0+\tau_c$ in longitudinal and transverse directions in table 3 are estimated by the following (C3) and (C4), respectively:

$$\sigma_{x_i'(t_0)x_i'(t_0+\tau_c)} = \frac{\dfrac{1}{N_c}\displaystyle\sum_{i=1}^{N_c}(x_i'(t_0)-\overline{x_i'(t_0)})(x_i'(t_0+\tau_c)-\overline{x_i'(t_0+\tau_c)})}{\sqrt{\dfrac{1}{N_c}\displaystyle\sum_{i=1}^{N_c}\left(x_i'(t_0)-\overline{x_i'(t_0)}\right)^2}\sqrt{\dfrac{1}{N_c}\displaystyle\sum_{i=1}^{N_c}\left(x_i'(t_0+\tau_c)-\overline{x_i'(t_0+\tau_c)}\right)^2}}, \tag{C3}$$

$$\sigma_{y_i'(t_0)y_i'(t_0+\tau_c)} = \frac{\dfrac{1}{N_c}\displaystyle\sum_{i=1}^{N_c}y_i'(t_0)y_i'(t_0+\tau_c)}{\sqrt{\dfrac{1}{N_c}\displaystyle\sum_{i=1}^{N_c}y_i'(t_0)y_i'(t_0)}\sqrt{\dfrac{1}{N_c}\displaystyle\sum_{i=1}^{N_c}y_i'(t_0+\tau_c)y_i'(t_0+\tau_c)}}. \tag{C4}$$

Here, N_c is the number of Lagrangian particles inside the computational domain at $t_0+\tau_c$.

References

Abderrahmane, H.A., Paquet, F. & Ng, H.D. 2011 Applying nonlinear dynamics theory to one-dimensional pulsating detonations. *Combust. Theor. Model.* **15**, 205–225.

Anand, V. & Gutmark, E. 2019 Rotating detonation combustors and their similarities to rocket instabilities. *Prog. Energy Combust. Sci.* **73**, 182–234.

Austin, J.M. 2003 The role of instability in gaseous detonation. PhD thesis, California Institute of Technology.

Austin, J.M., Pintgen, F. & Shepherd, J.E. 2005 Reaction zone in highly unstable detonations. *Proc. Combust. Inst.* **30**, 1849–1857.

Babiano, A., Basdevant, C., Roy, P.L. & Sadourny, R. 1990 Relative dispersion in two-dimensional turbulence. *J. Fluid Mech.* **214**, 535–557.

Boffetta, G., Celani, A., Crisanti, A. & Vulpiani, A. 1999 Pair dispersion in synthetic fully developed turbulence. *Phys. Rev.* E **60**, 6734–6741.

Boffetta, G. & Sokolov, I.M. 2002 Statistics of two-particle dispersion in two-dimensional turbulence. *Phys. Fluids* **14**, 3224–3232.

Borzou, B. 2016 Lagrangian trackers to investigate the detonation dynamics. http://detonationlab.blogspot.ca/2016/05/lagrangian-trackers-to-investigate.html.

Bourgoin, M., Ouellette, N.T., Xu, H., Berg, J. & Bodenschatz, E. 2006 The role of pair dispersion in turbulent flow. *Science* **311**, 835–838.

Buaria, D., Sawford, B.L. & Yeung, P.K. 2015 Characteristics of backward and forward two-particle relative dispersion in turbulence at different Reynolds numbers. *Phys. Fluids* **27**, 105101.

Buckmaster, J. 1989 A theory for triple point spacing in overdriven detonation waves. *Combust. Flame* **77**, 219–228.

Buckmaster, J.D. & Ludford, G.S.S. 1986 The effect of structure on the stability of detonations. I. Role of the induction zone. *Proc. Combust. Inst.* **21**, 1669–1676.

Chapman, S. & Cowling, T.G. 1991 *The Mathematical Theory of Non-uniform Gases*, 3rd edn. Cambridge University Press.

Chinnayya, A., Hadjadj, A. & Ngomo, D. 2013 Computational study of detonation wave propagation in narrow channels. *Phys. Fluids* **25**, 036101.

Chiquete, C. & Short, M. 2019 Characteristic path analysis of confinement influence on steady two-dimensional detonation propagation. *J. Fluid Mech.* **863**, 789–816.

Crane, J., Lipkowicz, J.T., Shi, X., Wlokas, I., Kempf, A.M. & Wang, H. 2023 Three-dimensional detoantion structure and its response to confinement. *Proc. Combust. Inst.* **39**, 2915–2923.

Crane, J., Shi, X., Lipkowicz, J.T., Kempf, A.M. & Wang, H. 2021 Geometric modeling and analysis of detonation cellular stability. *Proc. Combust. Inst.* **38**, 3585–3593.

Darragh, R., Towery, Z., Poludnenko, A.Y. & Hamlington, P.E. 2021 Particle pair dispersion and eddy diffusivity in a high-speed premixed flame. *Proc. Combust. Inst.* **38**, 2845–2852.

Desbordes, D. & Presles, H.N. 2012 Multi-scaled cellular detonation. In *Shock Waves Science and Technology Library* (ed. F. Zhang), vol. 6, pp. 281–338. Springer.

Eckett, C.A., Quirk, J.J. & Shepherd, J.E. 2000 The role of unsteadiness in direct initiation of gaseous detonations. *J. Fluid Mech.* **421**, 147–183.

Edwards, D.H., Jones, A.T. & Phillips, D.E. 1976 The location of the Chapman-Jouguet surface in a multiheaded detonation wave. *J. Phys.* D*: Appl. Phys.* **9**, 1331–1342.

Emmons, H.W. 1958 Flow discontinuities associated with combustion. In *Fundamentals of Gas Dynamics in High Speed Aerodynamics and Jet Propulsion* (ed. H.W. Emmons). Princeton University Press.

Faria, L.M. 2014 Qualitative and asymptotic theory of detonations. PhD thesis, King Abdullah University of Science and Technology.

Favre, A. 1965 Equation des gas turbulents compressibles. *J. Méc.* **4**, 361–421.

Ficket, W. & Davis, W.C. 2000 *Detonation Theory and Experiment*. Dover Publication.

Gamezo, V.N., Desbordes, D. & Oran, E.S. 1999*a* Formation and evolution of two-dimensional cellular structure. *Combust. Flame* **116**, 154–165.

Gamezo, V.N., Desbordes, D. & Oran, E.S. 1999*b* Two-dimensional reactive flow dynamics in cellular detonation waves. *Shock Waves* **9**, 11–17.

Gamezo, V.N., Vasil'ev, A.A., Khokhlov, A.M. & Oran, E.S. 2000 Fine cellular structure produced by marginal detonations. *Proc. Combust. Inst.* **28**, 611–617.

Gordon, S., McBride, B.J. & Zeleznik, F.J. 1984 Computer program for calculation of complex chemical equilibrium compositions and applications supplement I - transport properties. *NASA Tech. Rep.* 86885.

GOTTLIEB, S., SHU, C. & TADMOR, E. 2001 Strong stability-preserving high-order time discretization methods. *SIAM Rev.* **43**, 89–112.

GOU, X., SUN, W., CHEN, Z. & JU, Y. 2010 A dynamic multi-timescale method for combustion modeling with detailed and reduced chemical kinetic mechanism. *Combust. Flame* **157**, 1111–1121.

HAN, W., KONG, W., GAO, Y. & LAW, C.K. 2017 The role of global curvature on the structure and propagation of weakly unstable cylindrical detonations. *J. Fluid Mech.* **813**, 458–481.

HAN, W., WANG, C. & LAW, C.K. 2019 Role of transversal concentration gradient in detonation propagation. *J. Fluid Mech.* **865**, 602–649.

HENRICK, A.K., ASLAM, T.D. & POWERS, J.M. 2006 Simulations of pulsating one-dimensional detonations with true fifth order accuracy. *J. Comput. Phys.* **213**, 311–329.

HIGGINS, A. 2012 Steady one-dimensional detonations. In *Shock Waves Science and Technology Library* (ed F. Zhang), vol. 6, chap. 2, pp. 33–105. Springer.

HONG, Z., DAVIDSON, D.F. & HANSON, R.K. 2011 An improved H_2/O_2 mechanism based on recent shock tube/laser absorption measurements. *Combust. Flame* **158**, 633–644.

HU, F., WANG, R. & CHEN, X. 2016 A modified fifth-order WENOZ method for hyperbolic conservation laws. *J. Comput. Appl. Maths* **303**, 56–68.

JARSALÉ, G., VIROT, F. & CHINNAYYA, A. 2016 Ethylene-air detonation in water spray. *Shock Waves* **26**, 561–572.

JOURDAINE, J., TSUBOI, N. & HAYASHI, A.K. 2022 Investigation of liquid n-heptane/air spray detonation with an Eulerian-Eulerian model. *Combust. Flame* **244**, 112278.

JULLIEN, M., PARET, J. & TABELING, P. 1999 Richardson pair dispersion in two-dimensional turbulence. *Phys. Rev. Lett.* **82**, 2872–2875.

KANESHIGE, M. & SHEPHERD, J.E. 1997 Detonation database. *Tech. Rep.* FM97-8. Graduate Aeronautical Laboratories, California Institute of Technology.

KASIMOV, A.R. & STEWART, D.S. 2004 On the dynamics of self-sustained one-dimensional detonations: a numerical study in the shock-attached frame. *Phys. Fluids* **16**, 3566–3578.

KEE, R.J., COLTRIN, M.E. & GLARBORG, P. 2003 *Chemically Reacting Flow Theory and Practice*. Wiley.

KIM, K.H., KIM, C. & RHO, O. 2001 Methods for the accurate computations of hypersonic flows. I. AUSMPW+ scheme. *J. Comput. Phys.* **174**, 33–80.

KIYANDA, C.B. & HIGGINS, A.J. 2013 Photographic investigation into the mechanism of combustion in irregular detonation waves. *Shock Waves* **23**, 115–130.

LALCHANDANI, S. 2022 Modelling of quasi steady detonations with inert confinement. Master thesis, University of Ottawa.

LAU-CHAPDELAINE, S.S.-M., XIAO, Q. & RADULESCU, M.I. 2021 Viscous jetting and Mach stem bifurcation in shock reflections: experiments and simulations. *J. Fluid Mech.* **908**, A18.

LAW, C.K. 2006 *Combustion Physics*. Cambridge University Press.

LEE, J.H.S. 2008 *The Detonation Phenomenon*. Cambridge University Press.

LEE, J.H.S. & RADULESCU, M.I. 2005 On the hydrodynamic thickness of cellular detonations. *Combust. Explos. Shock Waves* **15**, 205–225.

MAXWELL, B.M., BHATTACHARJEE, R.R., LAU-CHAPEDLAINE, S.S.M., FALLE, S.A.E.G., SHARPE, G.J. & RADULESCU, M.I. 2017 Influence of turbulent fluctuation on detonation propagation. *J. Fluid Mech.* **818**, 646–696.

MAXWELL, B.M., PEKALSKI, A. & RADULESCU, M.I. 2018 Modelling of the transition of a turbulent shock-flame complex to detonation using the linear eddy model. *Combust. Flame* **192**, 340–357.

MAZAHERI, K., MAHMOUDI, Y. & RADULESCU, M.I. 2012 Diffusion and hydrodynamic instabilities in gaseous detonations. *Combust. Flame* **159**, 2138–2154.

MCBRIDE, B.J., GORDON, S. & RENO, M.A. 1993 Coefficients for calculating thermodynamic and transport properties of individual species. *NASA Tech. Rep.* 4513.

MÉVEL, R. & GALLIER, S. 2018 Structure of detonation propagating in lean and rich dimethyl ether-oxygen mixtures. *Shock Waves* **28**, 955–966.

MI, X., HIGGINS, A.J., NG, H.D., KIYANDA, C.B. & NIKIFORAKIS, N. 2017*b* Propagation of gaseous detonation waves in a spatially inhomogeneous reactive medium. *Phys. Rev. Fluids* **2**, 053201.

MI, X., TANG YUK, K.C., LEE, J.H.S., NG, H.D., HIGGINS, A.J. & NIKIFORAKIS, N. 2018 An approach to measure the hydrodynamic thickness of detonations in numerical simulations. In *37th International Symposium on Combustion. Dublin, Ireland*.

MI, X., TIMOFEEV, E.V & HIGGINS, A.J. 2017*a* Effect of spatial discretization of energy on detonation wave propagation. *J. Fluid Mech.* **817**, 306–338.

MÖLDER, S. 2016 Curved shock theory. *Shock Waves* **26**, 337–353.

MONNIER, V., RODRIGUEZ, V., VIDAL, P. & ZITOUN, R. 2022 An analysis of three-dimensional patterns of experimental detonation cells. *Combust. Flame* **245**, 112310.

MURRAY, S.B. & LEE, J.H. 1983 On the transformation of planar detonation to cylindrical detonation. *Combust. Flame* **52**, 262–289.

MURRAY, S.B. & LEE, J.H. 1985 The influence of yielding confinement on large-scale ethylene-air detonations. In *Dynamics of Shock Waves, Explosion, and Detonations* (ed. R.I. Soloukhin, A.K. Oppenheim, N. Manson & J.R. Bowen), pp. 80–103. American Institute of Aeronautics and Astronautics.

MURRAY, S.B. & LEE, J.H. 1986 The influence of physical boundaries on gaseous detonation waves. *Prog. Astronaut. Aeronaut.* **106**, 329–355.

NEUFELD, P.D., JANZEN, A.R. & AZIZ, R.A. 1972 Empirical equations to calculate 16 of the transport collision integral $\Omega^{(l,s)*}$ for the Lennard-Jones (12-6) potential. *J. Chem. Phys.* **57**, 1100–1102.

NG, H.D., HIGGINS, A.J., KIYANDA, C.B., RADULESCU, M.I., LEE, J.H.S., BATES, K.R. & NIKIFORAKIS, N. 2005*a* Nonlinear dynamics and chaos analysis of one-dimensional pulsating detonations. *Combust. Theor. Model.* **9**, 159–170.

NG, H.D., RADULESCU, M.I., HIGGINS, A.J., NIKIFORAKIS, N. & LEE, J.H.S. 2005*b* Numerical investigation of the instability for one-dimensioinal Chapman-Jouguet detonations with chain-branching kinetics. *Combust. Theor. Model.* **9**, 385–401.

ORAN, E.S., CHAMBERLAIN, G. & PEKALSKI, A. 2020 Mechanism and occurrence of detonation in vapor cloud explosions. *Prog. Energy Combust. Sci.* **77**, 100804.

PINTGEN, F., ECKETT, C.A., AUSTIN, J.M. & SHEPHERD, J.E. 2003 Direct observations of reaction zone in propagating detonations. *Combust. Flame* **133**, 211–229.

POLING, B.E., PRAUSNITZ, J.M. & O'CONNEL, J.P. 2001 *The Properties of Gases and Liquids*, 5th edn. McGraw-Hill.

RADULESCU, M.I. 2003 The propagation and failure mechanism of gaseous detonations: experiments in porous-walled tubes. PhD thesis, McGill University.

RADULESCU, M.I. 2018 A detonation paradox: why inviscid detonation simulations predict the incorrect trend for the role of instability in gaseous cellular detonations? *Combust. Flame* **195**, 151–162.

RADULESCU, M.I. & LEE, J.H.S. 2002 The faillure mechanism of gaseous detonations: experiment in porous wall tube. *Combust. Flame* **131**, 29–46.

RADULESCU, M.I., SHARPE, G.J. & BRADLEY, D. 2013 A universal parameter quantifying explosion hazards, detonability and hot spot formation: the χ number. In *Proc. of the Seventh International Seminar on Fire & Explosion Hazards* (ed. D. Bradley, G. Makhviladze, V. Molkov, P. Sunderland & F. Tamanini), pp. 1–13. Research Publishing.

RADULESCU, M.I., SHARPE, G.J., LAW, C.K. & LEE, J.H.S. 2007 The hydrodynamic structure of unstable cellular detonations. *J. Fluid Mech.* **580**, 31–81.

RADULESCU, M.I., SHARPE, G.J., LEE, J.H.S., KIYANDA, C.B., HIGGINS, A.J. & HANSON, R.K. 2005 The ignition mechanism in irregular structure gaseous detonations. *Proc. Combust. Inst.* **30**, 1859–1867.

REACTION DESIGN 2000 Transport: a software package for the evaluation of gas-phase, multicomponent transport properties. TRA-036-1.

REYNAUD, M., TAILEB, S. & CHINNAYYA, A. 2020 Computation of the mean hydrodynamic structure of gaseous detonation with losses. *Shock Waves* **30**, 645–669.

REYNAUD, M., VIROT, F. & CHINNAYYA, A. 2017 A computational study of the interaction of gaseous detonation with a compressible layer. *Phys. Fluids* **29**, 056101.

RICHARDSON, L.F. 1926 Atmospheric diffusion shown on a distance-neighbour graph. *Proc. R. Soc. Lond.* A **110**, 709–737.

ROMICK, C.M., ASLAM, T.D. & POWER, J.M. 2012 The effect of diffusion on the dynamics of unsteady detonations. *J. Fluid Mech.* **699**, 453–464.

SALAZAR, J.P.L.C. & COLLINS, L.R. 2009 Two-particle dispersion in isotropic turbulent flows. *Annu. Rev. Fluid Mech.* **41**, 405–432.

SAWFORD, B. 2001 Turbulent relative dispersion. *Annu. Rev. Fluid Mech.* **33**, 289–317.

SAWFORD, B.L., POPE, S.B. & YEUNG, P.K. 2013 Gaussian Lagrangian stochastic models for multi-particle dispersion. *Phys. Fluids* **25**, 055101.

SCATAMACCHIA, R., BIFERALE, L. & TOSCHI, F. 2012 Extreme events in the dispersions of two neighboring particles under the influence of fluid turbulence. *Phys. Rev. Lett.* **109**, 144501.

SHARPE, G.J. 2002 Shock-induced ignition for a two-step chain-branching kinetics model. *Phys. Fluids* **14**, 4372–4388.

SHEPHERD, J.E. 2009 Detonation in gases. *Proc. Combut. Inst.* **32**, 83–98.

SHI, L., SHEN, H., ZHANG, P., ZHANG, D. & WEN, C. 2017 Assessment of vibrational non-equilibrium effect on detonation cell size. *Combust. Sci. Technol.* **189**, 841–853.

SHIMURA, K. & MATSUO, A. 2018 Two-dimensional CFD-DEM simulation of vertical shock wave-induced dust lifting process. *Shock Waves* **28**, 1285–1297.

SHORT, M. & QUIRK, J.J. 2018 High explosive detonation-confiner interactions. *Annu. Rev. Fluid Mech.* **50**, 215–242.

SOKOLOV, I.M. 1999 Two-particle dispersion by correlated random velocity fields. *Phys. Rev.* E **60**, 5528–5532.

SOW, A., CHINNAYYA, A. & HADJADJ, A. 2014 Mean structure of one-dimensional unstable detonations with friction. *J. Fluid Mech.* **743**, 503–533.

SOW, A., CHINNAYYA, A. & HADJADJ, A. 2015 Computational study of non-ideal and mildly-unstable detonation waves. *Comput. Fluids* **119**, 47–57.

SOW, A., CHINNAYYA, A. & HADJADJ, A. 2019 On the viscous boundary layer of weakly unstable detonations in narrow channels. *Comput. Fluids* **179**, 449–458.

SOW, A., LAU-CHAPDELAINE, S.M. & RADULESCU, M.I. 2021 The effect of the polytropic index γ on the structure of gaseous detonations. *Proc. Combust. Inst.* **38**, 3633–3640.

STEWART, D.S. & KASIMOV, A.R. 2005 Theory of detonation with an embedded sonic locus. *SIAM J. Appl. Maths* **66**, 384–407.

STREHLOW, R.A. 1970 Multi-dimensional detonation wave structure. *Astronaut. Acta* **15**, 345–357.

TAILEB, S. 2020 Vers des simulations numériques prédictives des détonations gazeuses - Influence de la cinétique chimique, de l'équation d'état et des effets tridimensionnels. PhD thesis, ISAE-ENSMA.

TAILEB, S., MELUGUIZO-GAVILANCES, J. & CHINNAYYA, A. 2021*a* Influence of the chemical modeling on the quenching limits of gaseous detonation waves confined by an inert layer. *Combust. Flame* **218**, 247–259.

TAILEB, S., MELUGUIZO-GAVILANCES, J. & CHINNAYYA, A. 2021*b* The influence of the equation of state on the cellular structure of gaseous detonations. *Phys. Fluids* **33**, 036105.

TAILEB, S., REYNAUD, M., CHINNAYYA, A., VIROT, F. & BAUER, P. 2018 Numerical study of 3D gaseous detonations in a square channel. *Aerotec. Missili Spaz.* **97**, 96–102.

TANG, J. & RADULESCU, M.I. 2013 Dynamics of shock induced ignition in Fickett's model: influence of χ. *Proc. Combust. Inst.* **34**, 2035–2041.

TAYLOR, B.D., KESSLER, D.A., GAMEZO, V.N. & ORAN, E.S. 2013 Numerical simulations of hydrogen detonations with detailed chemical kinetics. *Proc. Combust. Inst.* **34**, 2009–2016.

VASILEV, A.A. & NIKOLAEV, Y. 1978 Closed theoretical model of a detonation cell. *Acta Astronaut.* **5**, 983–996.

VASIL'EV, A.A., GAVRILENKO, T.P., MITROFANOV, V.V., SUBBOTIN, V.A. & TOPCHIYAN, M.E. 1972 Location of the sonic transition behind a detonation front. *Combust. Explos. Shock Waves* **8**, 80–84.

WARNATZ, J., MAAS, U. & DIBBLE, R.W. 2006 *Combustion: Physical and Chemical Fundamentals, Modeling and Simulation, Experiments, Pollutant Formation*, 4th edn. Springer.

WATANABE, H. 2020 Gaseous detonation with dilute water spray in a two-dimensional straight channel: analysis based on numerical simulation. PhD thesis, Keio University.

WATANABE, H., MATSUO, A., CHINNAYYA, A., MATSUOKA, K., KAWASAKI, A. & KASAHARA, J. 2020 Numerical analysis of the mean structure of gaseous detonation with dilute water spray. *J. Fluid Mech.* **887**, A4.

WATANABE, H., MATSUO, A., CHINNAYYA, A., MATSUOKA, K., KAWASAKI, A. & KASAHARA, J. 2021 Numerical analysis on behavior of dilute water droplets in detonation. *Proc. Combust. Inst.* **38**, 3709–3716.

WATANABE, H., MATSUO, A., MATSUOKA, K., KAWASAKI, A. & KASAHARA, J. 2019 Numerical investigation on propagation behavior of gaseous detonation in water spray. *Proc. Combust. Inst.* **37**, 3617–3626.

WEBER, M. & OLIVIER, H. 2003 The thickness of detonation waves visualised by slight obstacles. *Shock Waves* **13**, 351–365.

WILKE, C.R. 1958 A viscosity equation for gas mixtures. *J. Chem. Phys.* **18**, 517–519.

WOLANSKI, P. 2013 Detonative propulsion. *Proc. Combust. Inst.* **34**, 125–158.

XIA, H., FRANCOIS, N., FABER, B., PUNZMANN, H. & SHATS, M. 2019 Local anisotropy of laboratory two-dimensional turbulence affects pair dispersion. *Phys. Fluids* **31**, 025111.

XIAO, Q. & RADULESCU, M.I. 2020 Dynamics of hydrogen-oxygen-argon cellular detonations with a constant mean lateral strain rate. *Combust. Flame* **215**, 437–457.

ZHANG, F. 2012 *Detonation Dynamics, Shock Wave Science and Technology Reference Library*. Springer.

ZHOU, Y., ZHANG, X., ZHONG, L., DEITERDING, R., ZHOU, L. & WEI, H. 2022 Effects of fluctuation in concentration on detonation propagation. *Phys. Fluids* **34**, 076101.